Combustion and Flame 208 (2019) 122–138

Contents lists available at ScienceDirect

Combustion and Flame

journal homepage: www.elsevier.com/locate/combustflame

A post processing technique to predict primary particle size of sooting flames based on a chemical discrete sectional model: Application to diluted coflow flames

Agnes Livia Bodor[a,b,*], Benedetta Franzelli[b], Tiziano Faravelli[a], Alberto Cuoci[a]

[a] CRECK Modeling Lab, Department of Chemistry, Materials, and Chemical Engineering, Politecnico di Milano, Piazza Leonardo da Vinci 32, Milano 20133, Italy

[b] Laboratoire EM2C CNRS, CentraleSupélec, Université Paris-Saclay, Gif-sur-Yvette, France

ARTICLE INFO

Article history:
Received 10 December 2018
Revised 7 June 2019
Accepted 10 June 2019

Keywords:
Soot
Primary particle
Discrete sectional soot model
Coflow flame
Co-flow flame
Premixed flame

ABSTRACT

A numerical post-processing strategy to reconstruct the size of soot primary particles is presented in this work in the context of the chemical sectional models. The proposed technique is based on solving the transport equation of the primary particle number density for each considered aggregate size. The chemical source terms are derived from the corresponding chemical reactions.

The validity of the proposed approach is tested on target flames of the International Sooting Flame (ISF) Workshop. In particular, first, a laminar premixed ethylene flame is considered. Profiles of soot volume fraction and mean primary particle size are compared between simulation and measurements and a satisfactory agreement is observed, validating the proposed post-processing strategy. Second, a laminar coflow ethylene flame is put under the scope. Numerical results are compared to experimental data once again in terms of soot volume fraction and primary particle size. The sensitivity to model parameters, such as accounting for surface rounding and the choice of the smallest aggregating particle size, is explored.

Once validated, the effect of dilution on the mean primary particle diameter in laminar diffusion flames is examined. The general trends observed experimentally are recovered. The correlation between temperature, precursor concentrations, soot volume fraction and primary particle diameter is explored. Finally, formation rates and residence time along the particle trajectories are investigated to explain the effect of dilution on the spatial localization of the biggest particles along the flame. The relation between the soot volume fraction and the mean primary particle diameter is examined.

1. Introduction

The control of soot (or particulate matter – PM) production by human activity or forest fires is one of the main concerns for the combustion community in terms of environmental protection for many reasons. For example, high absorption of visible or near-infrared light by soot particles is believed to be related to global warming due to the increased radiative forcing [1]; the soot deposit on snow increases the light absorption and decreases the reflection, consequently accelerating the melting process [2]; aerosols emitted into the atmosphere can cause or enhance respiratory, cardiovascular, infectious and allergic diseases [3]. All these processes depend not only on the number of particles and their total mass, but also on their size and, in particular, on their surface [4].

Despite the importance of particle surface, numerical and experimental tools for the characterization of this key quantity still have to be improved. This is mainly due to the complexity of the problem since soot particles are the result of numerous local chemical and collisional processes leading to a population of particles of different size and morphology [5–8]. In particular, it is generally assumed that small particles have a spherical shape whereas large particles have a fractal-like nature and are composed of small, quasi-spherical identical building blocks of

* Corresponding author at: CRECK Modeling Lab, Department of Chemistry, Materials, and Chemical Engineering, Politecnico di Milano, Piazza Leonardo da Vinci 32, Milano, 20133 Italy.
E-mail address: agneslivia.bodor@polimi.it (A.L. Bodor).
URL: http://creckmodeling.chem.polimi.it (A.L. Bodor)

https://doi.org/10.1016/j.combustflame.2019.06.008

Nomenclature

Δx	mesh cell size in the radial direction
Δy	mesh cell size in the axial direction
$\dot{\Omega}$	chemical source term
$\dot{\omega}$	reaction specific chemical source term
$\mathbf{V}$	diffusion velocity
$\mathbf{v}$	flow velocity
μ	stoichiometric coefficient of formed species
ν	stoichiometric coefficient of reacting species
ρ	mixture density
ρ_{pp}	primary particle number density
ρ_{soot}	soot density
BIN	soot section
C_{r}	correction constant for surface rounding
d_{amean}	arithmetic mean diameter
d_{CMD}	count median diameter
d_{geom}	geometrical mean diameter
d_{mono}	mean d_{pp} derived with assuming monodisperse distribution
d_{pp}	primary particle diameter
$d_{\mathrm{pp},N_{\mathrm{min}}}$	diameter of the smallest soot particle accounted in d_{mean} calculation
$d_{\mathrm{pp},N_{\mathrm{s}}}$	diameter of the smallest aggregating particle
f_{v}	soot volume fraction
h	Planck constant
M	molecular weight
N_{Av}	Avogadro constant
N_{a}	number of aggregate soot sections
N_{g}	number of gaseous species
n_{pp}	primary particle number per aggregate
N_{s}	index of smallest BIN with solidified particles
R	reaction rate
S	aggregate surface
S_{Birth}	birth rate of primary particles
S_{Death}	consumption rate of primary particles
V	aggregate volume
X	non-aggregate chemical species
Y	species mass fraction

Glossary

PPSD	Primary Particle Size Distribution
ISF	International Sooting Flame
PSD	Particle Size Distribution
MOM	Method of Moments
ADSM	Aerosol Discrete Sectional Model
CDSM	Chemical Discrete Sectional Model
F32	ISF coflow laminar flame 3 with 32% volumetric ethylene content
F40	ISF coflow laminar flame 3 with 40% volumetric ethylene content
F60	ISF coflow laminar flame 3 with 60% volumetric ethylene content
F80	ISF coflow laminar flame 3 with 80% volumetric ethylene content
PBE	Population Balance Equation
LII	Laser-Induced Incandescence
TIRELII	Time-Resolved Laser-Induced Incandescence
RR	Resonance Stabilized Radicals
YDB	Yale Diffusion Burner
PAH	Polycyclic Aromatic Hydrocarbons

diameter d_{pp}, called primary particles. Once the volume (V) of one aggregate and the d_{pp} are known, the surface area can be obtained as $S = 6Vd_{\mathrm{pp}}^{-1}$. Therefore, in order to properly estimate the pollutant contribution of a burner, in addition to the classical particle size distribution (PSD), it is essential to understand the evolution of the primary particle size distribution (PPSD) along a flame and to correctly model it.

Concerning the numerical models, most of them are limited to predict exclusively the PSD [9–15]. In general, modeling the primary particle size is a challenging and computationally expensive task. For this, the description of soot particles has to be bivariate as, beside the mass or the volume, an additional variable (surface, primary particle size or primary particle number) has to be tracked, resulting in a two-dimensional distribution function.

Among the different available descriptions, the Monte Carlo (MC) approach is a very accurate statistical technique capable to predict soot particles evolution, including information on their shape. MC simulations were performed by several researchers [16–19], but they are limited to zero or one-dimensional cases [16–23] due to their high computational cost.

Recently, alternative numerical soot models were extended to access information about primary particle diameter (d_{pp}) like the method of moments (MOM) and the sectional model.

The method of moments, originally suggested by Frenklach and Harris [24], is based on the transport of the moments of the PSD function. This model has been extended by Mueller et al. [25,26] to a bivariate version capable of providing information about the primary particle size. Alternative bivariate MOMs have been developed by Yuan et al. [27,28]. This family of modeling methods [29–35] has been applied on premixed laminar flames [22,29,36–38], on counterflow and coflow flames [29,36] and on turbulent flames [34,39] to investigate d_{pp}. However, the bivariate MOM models available in literature do not provide direct access to the PPSD, which is the long term objective of this work.

A promising alternative approach for soot prediction is the sectional soot model. Based on the way of treating the soot particle interactions, two types of sectional models can be distinguished: the aerosol discrete sectional models (ADSM) and the chemical discrete sectional models (CDSM). For both, the mass spectrum of soot particles are divided into discrete sections, each of them being representative of aerosol particles (ADSM) or chemical species (CDSM) in a given mass range.

Classically, the ADSM models are based on assuming spherical particles [13,40,41]. Only recently, the approach has been extended to obtain information on PPSD by transporting an additional variable [14,42,43]. The new variable can be either the particle surface [43] or the primary particle number [14,42,44–51]. Such extension may drastically increase the computational cost. Additionally, multiple subsections per mass section can be considered to account for the polydispersed character of d_{pp} in aggregates with a given size as done by Nakaso et al. [52] for titania nanoparticles. However, the associated computational cost is too high for multi-dimensional problems. Alternatively, to predict the primary particle size with the aerosol sectional model a volume-surface relation can be presumed [53]. However, even if such an approach do not increase the CPU cost of the sectional method, it should be noticed that the presumed volume-surface law is not general. In addition, it can be shown that the law proposed in [53] implicitly models aggregates as composed by primary particles with a given constant diameter, corresponding to the diameter of the biggest spherical particles allowed by this law. Therefore, it can be expected that the evolution of the primary particle diameter for aggregate is not correctly accounted for.

Concerning the chemical sectional soot approach, several models were developed and used for soot formation modeling in the last decade [13,14,40,41,54–58]. These models solve a conservation equation for each species' molar concentration or mass fraction. The interaction between two representative species of the soot sections (BINs) or a BIN and a gaseous species is described by a

chemical reaction. The reaction rates are determined through the Arrhenius' equation. The rate constants are derived from reference reactions and are usually similar if they belong to the same type of formation process: soot inception, Hydrogen-Abstraction-Carbon-Addition (HACA), surface growth, Polycyclic Aromatic Hydrocarbon (PAH) condensation, dehydrogenation, coalescence or oxidation [56]. The differences between these processes are therefore incorporated in the kinetic mechanism. Usually, the chemical sectional model also includes subsections to distinguish between BINs with different H/C ratio, level of dehydrogenation [56,57]. This expansion of the mechanism with subsection provides more information and an improved description but also increased computational cost. Currently, the CDSMs assume either spherical molecules for all sections [13,40,41] or spherical molecules for small particles below a critical particle size and constant primary particle size for larger particles, i.e. aggregates [56]. The extension of CDSM to a bivariate version (particle size-primary particle size) is possible and it provides a new perspective to the kinetic mechanism validation. Furthermore, access to the reaction rates and the PPSD can help to reveal which conditions and formation processes result in particles with large surfaces.

In this context, the objectives of this work are twofold. The first, main objective is to present a general post-processing model for CDSM suitable to obtain information on the mean primary particle diameter and test its performance while coupled with a state-of-the-art CDSM. For this, a new variable, the primary particle number density, is transported for each aggregate species. This extension adopts the same assumptions about the behavior of primary particles as done by Wen et al. [14], Park et al. [59] and Mueller et al. [25,26]. The model is incorporated into the detailed kinetic mechanism of the CRECK Modeling Group [56].

Here, the tracking procedure is used as a post-processing tool, meaning that new results on d_{pp} are not considered to recalculate the reaction rates. This neglected coupling may affect the result's accuracy, but it is here preferred in order to limit the computational cost. Coupled with the reaction kinetics, the simulations might get expensive, therefore coupling is a long term target. In addition, the use of the tracking procedure as a post-processing method allows to identify if big discrepancies are detected between the new d_{pp} predictions and the one based on the classical assumptions of CDSM methods. This may provide an indication of the need for accounting for the coupling in the future simulations of the considered flames.

The new tracking model is validated by considering two of the reference flames of the International Sooting Flame (ISF) Workshop [60]. In specific: the third premixed ISF target flame (ISF-premixed-laminar-3) and the third laminar coflow flame (ISF-coflow-laminar-3) with 80% ethylene content are considered.

After validating the model, the second objective is to study the variation of the primary particle size due to dilution with the help of the knowledge gained about the soot formation processes by a CDSM. For this, the full series of the ISF-coflow-laminar-3 flames (32% (F32), 40% (F40), 60% (F60) and 80% (F80) ethylene/nitrogen volume content in the fuel stream) is put under the scope. The variation of primary particle size is then explored.

The paper is organized as follows. In Section 2.1 the general primary particle tracking method for CDSM is presented and the transport equation of primary particle number density is derived. In Section 2.2 the kinetic mechanism of CRECK Modeling Group [56], used to perform the calculations, is briefly described. In Sections 3.1 and 3.2 the performance of the combined model is tested by comparing the numerical results to the available experimental data. The mean d_{pp} calculated with the new method is compared to the ones derived from former primary particle size assumptions of CDSMs (spherical particles and constant primary particle size in the aggregates). Parallel to the validation, the result's sensitivity to the model parameters is discussed. Finally, the effect of dilution on the primary particle size is discussed in Section 4 for the ISF-coflow-laminar-3 flame series.

2. Model description

In this section, the general model for determining the primary particle size in the aggregate BIN sections of a CDSM is presented. The new variable, the primary particle number density (ρ_{pp}), is introduced and the transport equation governing its evolution is derived. In Section 2.2, a short overview of the kinetic mechanism, in which the primary particle tracking was incorporated, is given.

2.1. Primary particle tracking for CDSMs

The pathway for the formation of aggregates used by the bivariate models mentioned in the previous section was originally suggested by Lahaye [6]. It assumes that first a multitude of small particles are formed. Second, their growth or collision result in larger, but still spherical particles that solidify later on. Finally, the collision of the solidified particles produces aggregates. These can grow larger by further aggregation, by condensation or surface growth.

Following the model of Lahaye [6], particles below the solidification limit (BIN_i, $i < N_s$) are considered to coalesce completely, resulting in spherical molecules, whereas pure aggregation is assumed between particles larger or equal to the limit (for BIN_i, $i \geq N_s$).

The interactions of small and big particles are taken as a splash of the former on the latter distributing its mass homogeneously on the surface. This last interaction, similarly to obliteration, leads to a more spherical shape, thickening the connection of primary particles [17,18,43]. In the following, the shape modifications leading to increased sphericity will be referred to as "surface rounding" regardless of the process' type.

The new variable, the so-called primary particle number density ($\rho_{pp,i}$), is defined for each soot section and represents the number of primary particles of type BIN_i per mass unit. For not solidified (spherical) particles the primary particle number density can be derived from the molecular weight (M_i) and the mass fraction (Y_i) as:

$$\rho_{pp,i} = \frac{Y_i N_{Av}}{M_i} \qquad i \leq N_s \tag{1}$$

where N_{Av} is the Avogadro constant. Therefore, no additional transport equation needs to be solved for BIN_i with $i < N_s$.

ρ_{pp,N_s} is the primary particle number density for the smallest particle colliding without coalescence. This particle is still considered spherical as it was formed by coalescence or surface growth, therefore ρ_{pp,N_s} can be derived by Eq. (1).

The primary particles are assumed to possess the same chemical, thermal and transport properties as the representative species of the section, therefore the conservation equation for the aggregate BINs (BIN_i $i > N_s$) takes the following form:

$$\frac{\partial}{\partial t}(\rho\rho_{pp,i}) + \nabla\cdot(\rho\rho_{pp,i}\mathbf{v}) = -\nabla\cdot(\rho\rho_{pp,i}\mathbf{V_i}) + \dot{\Omega}_{pp,i} \tag{2}$$

where ρ is the density of the mixture, $\mathbf{v}$ is the velocity, $\mathbf{V_i}$ is the diffusion velocity of the BIN_i [61] and $\dot{\Omega}_i$ is the chemical reaction source term. Due to the high Schmidt number characterizing the soot particles [62], the contribution of molecular diffusion is negligible. Only thermal diffusion plays a significant role [63] and was included in the transport equation.

The chemical reaction source term is the sum of contributions of each reaction related to BIN_i ($\dot{\omega}_{l,i}$), which is the result of the sink ($S_{Death,l,i}$) and the formation ($S_{Birth,l,i}$) terms of the specific

reaction:

$$\dot{\Omega}_{pp,i} = \sum_l \dot{\omega}_{l,i} = \sum_l \left(S_{Death,l,i} + S_{Birth,l,i}\right) \tag{3}$$

where l is the index of the reaction. The formation rate is a function of all the reaction rates (R) in which BIN_i is involved, as described in details in the following.

The source term depends only on the primary particle number of particles colliding without coalescence and can be determined for a general reaction of shape:

$$\sum_{i=N_s}^{N_s+N_a} \nu_i BIN_i + \sum_{i=1}^{N_s-1} \nu_i BIN_i + \sum_{j=1}^{N_g} \nu_j X_j \Rightarrow \sum_{i=N_s}^{N_s+N_a} \mu_i BIN_i + \sum_{i=1}^{N_s-1} \mu_i BIN_i + \sum_{j=1}^{N_g} \mu_j X_j \tag{4}$$

where X are gaseous species, N_g is the number of gaseous species, N_a is the number of aggregate BINs, ν_i and μ_i are the stoichiometric coefficients. Regarding the change in the primary particle number only the first terms on the two sides of the reactions are relevant, as coalescing BINs and gaseous species do not affect the primary particle number of the aggregates directly.

The primary particle number in the ith aggregate BIN species ($n_{pp,i}$) can be expressed by:

$$n_{pp,i} = \frac{M_i \rho_{pp,i}}{Y_i N_{Av}} \tag{5}$$

The consumption of BIN_i type primary particles originating from reaction l can be expressed as:

$$S_{Death,l,i} = -\frac{\nu_i M_i \rho_{ppi}}{Y_i} R_l \tag{6}$$

where R_l is expressed in molar units.

The total number of new particles resulted from reaction l is the sum of the original particles (LHS of the reaction) multiplied by the term $(1 - C_r)$ to account for the surface rounding phenomenon, with C_r being the correction factor derived later. Consequently, the total source term ($S_{Birth,l}$) for the birth of the primary particles by reaction l is expressed as:

$$S_{Birth,l} = \sum_{k=N_s}^{N_s+N_a} (1 - C_r) \frac{\nu_k M_k \rho_{PBk}}{Y_k} R_l \tag{7}$$

The born primary particles are distributed among the resultant large BINs conserving the average primary particle mass similarly to the model of Thompson and coworkers [14]. Therefore, the resultant chemical source term can be written in the form:

$$\dot{\omega}_{l,i} = \underbrace{\frac{\mu_i M_i}{\sum_{k=N_s}^{N_s+N_a} \mu_k M_k} \sum_{j=N_s}^{N_s+N_a} (1 - C_r) \frac{\nu_j M_j \rho_{pp,j}}{Y_j} R_l}_{S_{Birth,l,i}} - \underbrace{\frac{\nu_i M_i \rho_{pp,i}}{Y_i} R_l}_{S_{Death,l,i}} \tag{8}$$

A drawback of this type of primary particle assignment to the resultant species is that all new primary particles have the same size, causing a narrower PPSD. However the mean primary particle mass is conserved.

In the current model, the primary particles are assumed to have point contact within a soot particle at all instance. Actually, surface rounding would increase the area of contact between neighboring primary particles, partially merging them. Therefore, in order to account for the above-mentioned merge of primary particles, the primary particle number should decrease, which is realized by C_r.

The correction factor is derived from the assumption of Patterson and Kraft [43], i.e. the change of the particle surface area (dS) for a deposited dV volume is related to the initial surface S_{init}:

$$\frac{dS}{dV} = 2\left(\frac{S_{init}}{4\pi}\right)^{-1/2} \tag{9}$$

The deposited volume can be obtained for the general reaction as:

$$dV = \frac{1}{\rho_{soot}} \left(\sum_{i=N_s}^{N_s+N_a} \nu_i M_i - \sum_{i=N_s}^{N_s+N_a} \mu_i M_i \right) \tag{10}$$

where ρ_{soot} is the soot density.

Changing the variable from surface to primary particle number, the correction factor takes the form:

$$C_r = \frac{2}{V_{init} n_{pp,init}} \left(1 - \frac{1}{\sqrt{n_{pp,init}}}\right) \tag{11}$$

where V_{init} and $n_{pp,init}$ are the initial volume and primary particle number of the molecules.

Three different characteristic diameters may be extracted from the obtained PPSD: the arithmetic mean diameter (d_{amean}), the geometrical mean diameter (d_{geom}) – which is equal to the count median diameter (d_{CMD}) in case of a lognormal distribution – and a diameter assuming monodisperse distribution while preserving the total soot mass and primary particle number (d_{mono}). They are defined as follows:

$$d_{amean} = \frac{\sum_{k=N_{min}}^{N_{max}} d_{pp,k} \rho_{pp,k}}{\sum_{k=N_{min}}^{N_{max}} \rho_{pp,k}} \tag{12}$$

$$d_{geom} = \left(\prod_{k=N_{min}}^{N_{max}} (d_{pp,k})^{\rho_{pp,k}} \right)^{1/\prod_{k=N_{min}}^{N_{max}} \rho_{pp,k}} \tag{13}$$

$$d_{mono} = \left(\frac{6}{\pi \rho_{soot}} \frac{\sum_{k=N_{min}}^{N_{max}} Y_k}{\sum_{k=N_{min}}^{N_{max}} \rho_{pp,k}} \right)^{1/3} \tag{14}$$

where N_{max} and N_{min} are the indexes of largest and smallest BIN considered to calculate the mean diameter, respectively. This also determines the low cut-off size, i.e. the smallest particle accounted ($d_{pp,N_{min}}$) to calculate the mean diameter. This quantity is not a parameter of the post-processing procedure. As it will be shown in the following, its value may affect the obtained numerical results on the mean primary particle diameter, whereas the soot volume fraction is only slightly dependent on this quantity (since small particles do not largely contribute to the total mass). Unfortunately, the experimental $d_{pp,N_{min}}$ value is often unknown so that uncertainties on this quantity has to be kept in mind when performing the comparison between experimental and numerical data.

2.2. Detailed kinetic mechanism

The above-described model was incorporated into the kinetic mechanism of the CRECK Modeling Group [56], which includes 189 gaseous species and a sectional soot model with 20 sections. In this work, the kinetic mechanism was extended with 4 further mass sections in order to cover the aggregate size range in the heavily sooting flames. This sectional model splits up the large hydrocarbon species primarily based on mass and secondary based on H/C ratio. 3 H/C subsections are assigned for heavy PAHs (from BIN_1 to BIN_4) and soot particles from BIN_5 to BIN_{10} and 2 H/C subsections for BIN_{11} and BIN_{10} and soot aggregates (from BIN_{13} to BIN_{20}). The result is 50 subsections resulting in 100 species to describe the PAHs and soot particles, due to the separate treatment for radicals and molecules. Each new section (BIN_{21} to BIN_{24}) has 2 H/C subsections with the hydrogenation levels defined for BIN_{20}, and the original spacing between the BINs is kept.

In its original form, the kinetic mechanism considers soot particles as spheres and soot aggregates as an assembly of uniform

sized primary particles, with the size of the last spherical particle (BIN_{12}, i.e. $\sim$10 nm) and a fractal dimension of 1.8.

2.3. Kinetic mechanism extension with primary particle tracking

The above described chemical mechanism was extended by including the tracking of primary particles. To keep the consistency, $N_s = 12$ is taken for the primary particle calculations, i.e. the smallest aggregating particle has a diameter of $\sim$10 nm ($d_{pp,N_s} \approx$ 10 nm). It means that one primary particle per molecule was assumed for BINs smaller or equal to BIN_{12} (spherical particle assumption) and the transport equation was solved only for the aggregate BINs (BIN_i $i > 12$).

As already said, the implementation of the primary particle tracking was done without the two-way coupling between d_{pp} and the kinetic mechanism, i.e. the change of the primary particle size was not considered in the reaction kinetics, calculated from the original assumption ($d_{pp} \approx$ 10 nm). According to Patterson and Kraft [43] the error introduced by neglecting this coupling is moderate compared to the imperfection of the kinetic mechanism, once the aggregate nature is considered. However, this cannot be considered valid for every kinetic mechanism and condition, so that the error by neglecting the coupling cannot be quantified here. Nevertheless, the proposed method can provide a first estimation of the need for accounting for such coupling by highlighting the differences between the assumed and the calculated d_{pp}. Accounting for such coupling can be considered as a potential improvement of the model, but the quantification of its effect on the prediction of the soot volume fraction (f_v), of the PSD and the PPSD is outside of the scope of the current work.

3. Validation

In the following, the model combining the CRECK Modeling Group's kinetic mechanism [56] and the proposed primary particle tracker will be tested in a premixed laminar ethylene flame and in a coflow laminar ethylene diffusion flames. The numerical soot volume fraction and the mean primary particle size will be compared to the available experimental data to quantify its accuracy and to prove its interest compared to the "classical" description based on spherical particle assumption or considering constant primary particle size for aggregates.

3.1. Premixed ethylene/air flame

The model is here validated on a premixed flame. The ISF-premixed-laminar-3 was chosen for validation as it is the target flame for Laser-Induced Incandescence (LII) measurement, which can provide information on the primary particle size when the time-resolved evolution of the LII signal is considered [64–66]. Due to the simplicity of the flame, the simulation is easy to carry out and the performance of the new extended chemical model can be put under the focus without fearing errors potentially introduced by improper modeling of the flow field or of the flow-flame interaction. The measurement rig of the target flame [67–69] is a so-called McKenna burner producing a premixed flat ethylene/air flame with an equivalence ratio of $\Phi = 2.1$.

The numerical simulation was performed with the OpenSMOKE++ framework [70]. The inlet velocity and the species mass fractions were prescribed according to the experimental setup and the temperature profile was imposed as suggested by the ISF Workshop [60]. The numerical length of the domain was chosen equal to 4 cm, which is sufficient to minimize the effects of the outlet boundary conditions.

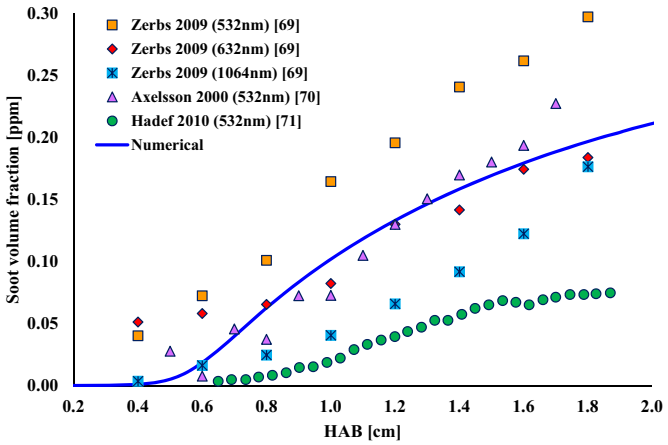

Fig. 1. Soot volume fraction comparison between experimental (marks) and numerical (solid line) results for the ISF-premixed-laminar-3 flame.

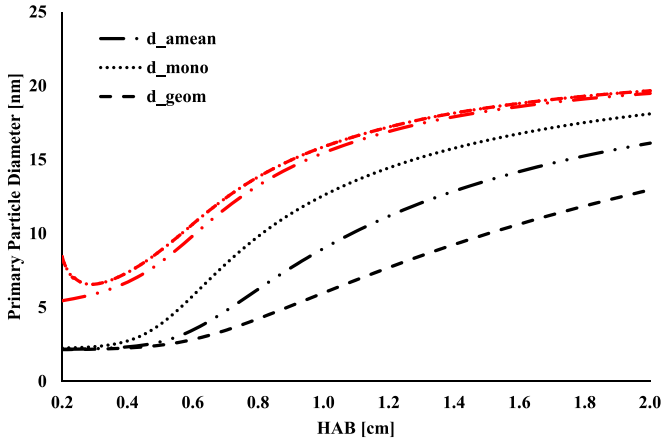

Fig. 2. Simulated d_{amean}, d_{mono} and d_{geom} for two values of the low cut-off size ($d_{pp,N_{min}} = 2$ nm in black and $d_{pp,N_{min}} = 5$ nm in red) for the ISF-premixed-laminar-3 flame. (For interpretation of the references to color in this figure legend, the reader is referred to the web version of this article.)

3.1.1. Results

In Fig. 1, experimentally measured soot volume fractions [69,71,72] are compared to the numerical results using $d_{pp,N_{min}} =$ 2 nm, i.e. considering that the smallest soot particle experimentally measured has a diameter of 2 nm. The wavelengths, used for the extinction-scattering measurements, are indicated in the brackets in the legend of Fig. 1. The deviations among the experimental results reach up to a factor of $\sim$6 in the upper flame region. The simulation result is then in reasonably good agreement with the measurements and follows the general trend, i.e. the soot volume fraction increases with the height above the burner (HAB).

The three mean diameters defined in Eqs. (12)–(14) have been extracted from the numerical PPSD using two low-cut-off sizes $d_{pp,N_{min}} = 2$ nm and $d_{pp,N_{min}} = 5$ nm. Results are plotted in Fig. 2 with both $d_{pp,N_{min}}$ values.[1] Figure 2 allows highlighting the differences between the possible definitions for the mean primary particle diameters (by comparing d_{amean}, d_{mono} and d_{geom}) as well as to investigate the effect of the choice of the $d_{pp,N_{min}}$ value, which depends on the sensitivity of the experimental technique and is often unknown.

[1] The choice of $d_{pp,N_{min}}$ has a marginal impact on the soot volume fraction compared to the experimental uncertainties, the maximum deviation between the two profiles was below 15 ppb.

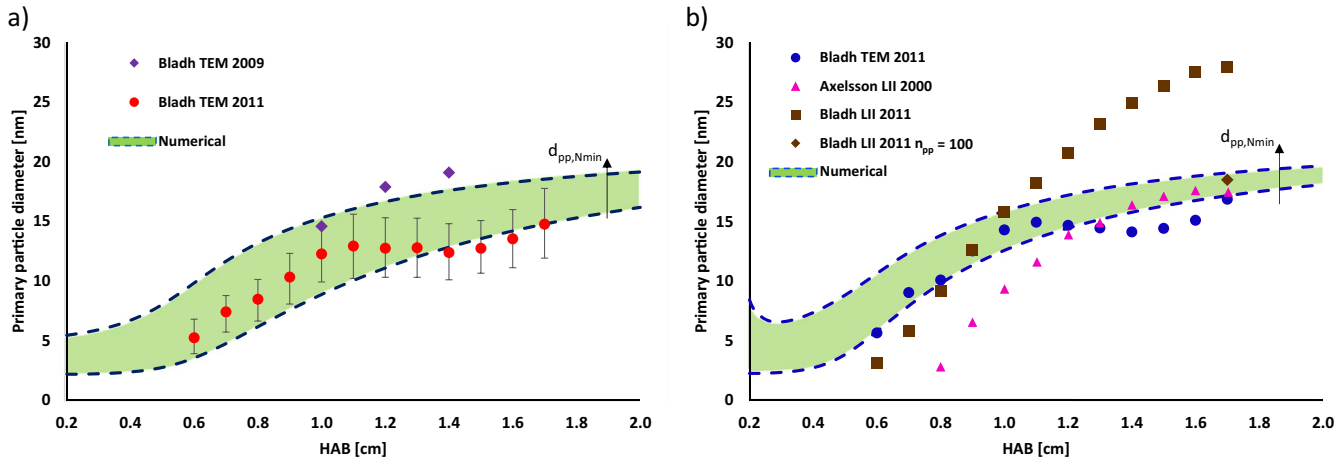

Fig. 3. Comparison between the experimentally determined [67–69] mean primary particle diameter and the numerical values (shaded area) (a) d_{amean} and (b) d_{mono} for the ISF-premixed-laminar-3 flame. (For interpretation of the references to color in this figure, the reader is referred to the web version of this article.)

A bimodal distribution with a significant amount of very small soot particles (2–5 nm) is classically observed for a wide range of conditions [12,73–75]. The current flame possesses a similar portray. Therefore, though the soot volume fraction only slightly differs by modifying the low cut-off size, the impact on the mean diameters is significant. This is important to recall when validation with experimental results is attempted. In the current flame, the numerically obtained distribution of particles above 5 nm is very narrow. Therefore, the three types of mean diameters are very similar for $d_{pp,N_{min}} = 5$ nm. On the contrary, for $d_{pp,N_{min}} = 2$ nm the three definitions differ significantly. In specific, the monodisperse assumption gives higher values than the arithmetic and the count mean diameter. This has to be kept in mind while performing validation with different measurement techniques, which may provide different characteristic diameters.

The profile of d_{mono} with $d_{pp,N_{min}} = 2$ nm shows an unexpected behavior, by decreasing in the zone close to the burner exit (at HAB = 0.2–0.3 cm). In this region the soot volume fraction is below 0.2 ppb and particles above 5 nm just start to evolve. As d_{mono} is calculated based on the particle volume, which is proportional to the 3rd power of the diameter, large particles largely contribute to d_{mono} compared to small particles, resulting in an unexpectedly large d_{mono} for this region.

It can be concluded that the choice of the correct $d_{pp,N_{min}}$ value may impact the results on the mean d_{pp}. However, it should be noticed that this parameter is not introduced by the proposed tracking procedure, but it is related to the experimental sensitivity, i.e. the capability of the experimental setup to capture small soot particles. On the one side, based on the study of Betrancourt et al. [76], soot particles as small as 2 nm can absorb laser energy and emit LII signal. While in a population with mainly small particles their signal can be detected, small particles' contribution to the LII signal in the presence of large particles is negligible, so that it is difficult to determine the exact value of $d_{pp,N_{min}}$ for LII measurements.

On the other side, the size of the smallest thermophoretically sampled particle detected by Transmission Electron Microscopy (TEM) depends on the optical apparatus and therefore can vary from setup to setup. De Iuliis et al. [77] highlight in their work the difficulty of capturing small particles. For the current flame, the distribution obtained with TEM by Bladh et al. [67] show no particles detected below 5 nm, but the lower detection limit is not explicitly defined. Therefore, when comparing the obtained numerical results to the experimental data, we need to account for such uncertainty.

Figure 3 shows the mean d_{pp} obtained by experiments with TEM [67,68] and LII [68,69] and the results of the numerical simulation. To account for the uncertainty of the smallest detected primary particle a range of possible mean diameters are derived by varying the $d_{pp,N_{min}}$ between 2 and 5 nm (green shaded area).

While from TEM measurements the arithmetic mean ("amean") was calculated, the diameters derived from the LII signals were experimentally obtained by assuming a monodisperse distribution ("mono") of self-standing particles without aggregate structure. To be consistent with the experimental definition, numerical results for d_{amean} and d_{mono} are presented for TEM and LII measurements, respectively. As TEM images were showing high primary particle number per aggregate in the upper flame region [68], an LII signal reevaluation with the assumption of 100 primary particles per aggregate was carried out by Bladh et al. [68] at HAB = 1.8 cm (this is marked by $n_{pp} = 100$ on Fig. 3). The mean diameter with the new assumption dropped from 28 to 18.5 nm indicating that LII signal evaluations without accounting for aggregate structure in this region probably intensively overestimate the mean primary particle diameter.

The diameters determined by Axelsson et al. [69] at HAB = 8 mm and by Bladh et al. [68] at HAB = 6 mm with LII are smaller than 5 nm, indicating that a significant amount of very small particles (2–5 nm) are present close to the burner, consequently the $d_{pp,N_{min}} = 2$ nm may be more appropriate in this region.

Before drawing final conclusions on the model's performance, the sensitivity to the model parameters, i.e. accounting or not for surface rounding and the size of the smallest aggregate d_{pp,N_s}, are investigated.

Sensitivity to model parameters

When applying the post-processing technique, surface rounding effects can be considered or not. In order to investigate the role of such a process on the results, Fig. 4 shows the deviance of the calculated mean diameters determined when neglecting the surface rounding. The effect of the correction term is negligible (below 3%) at all HABs for both $d_{pp,N_{min}}$ values and almost all diameter definitions. However, it plays an important role in the lower flame region (HAB ~0.3–0.7 mm) when calculating d_{mono} with $d_{pp,N_{min}} = 2$ nm.

Another key parameter of the post-processing model is d_{pp,N_s}, i.e. the size of the smallest aggregating particle. The smallest aggregating particle might differ from the one assumed in the presented calculations for consistency with the original CRECK model ($d_{pp,N_s} = 10$ nm). Therefore, the sensitivity to this parameter was investigated by modifying N_s to 10 and 14, resulting $d_{pp,N_s} \approx 6.4$

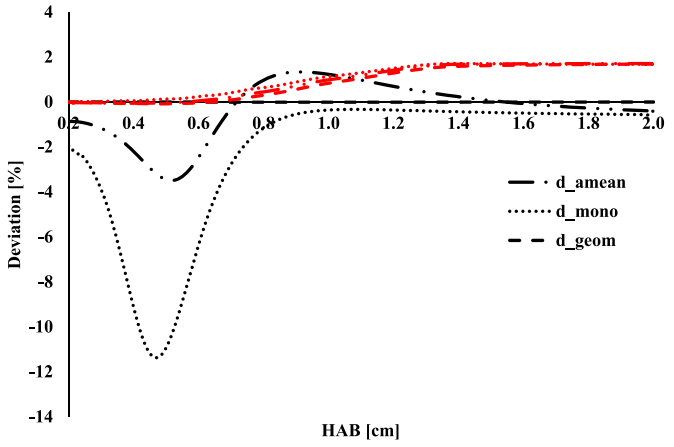

Fig. 4. Deviance of the calculated mean diameters determined when neglecting the surface rounding for the ISF-premixed-laminar-3 flame ($d_{pp,N_{min}} = 2$ nm in black $d_{pp,N_{min}} = 5$ nm in red). (For interpretation of the references to color in this figure legend, the reader is referred to the web version of this article.)

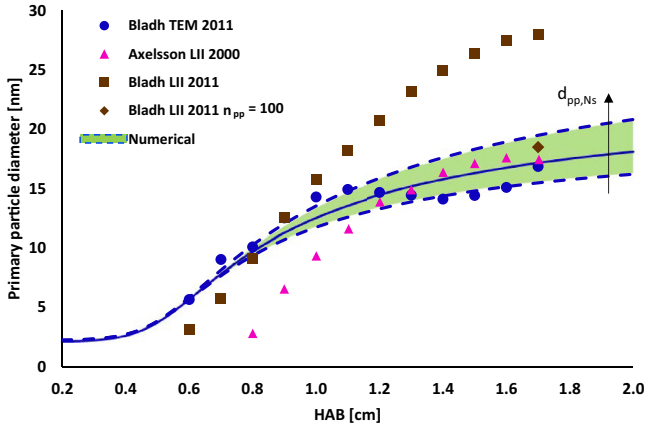

Fig. 5. Comparison between the experimentally determined d_{mono} with the numerical values (shaded area) for the ISF-premixed-laminar-3 flame: effect of the smallest aggregating particle diameter d_{pp,N_s} ($d_{pp,N_{min}} = 2$ nm). (For interpretation of the references to color in this figure legend, the reader is referred to the web version of this article.)

and 16 nm, respectively. A range of possible diameters (green shaded area) was determined in case of $d_{pp,N_{min}} = 2$ nm and represented in Fig. 5. A deviation of $\pm 15\%$ can be observed compared to the baseline (solid line). The profile of the distribution remains qualitatively the same.

Taking into account all the above considerations, the overall agreement between the numerical and the experimental results presented in Figs. 3 and 5 can be considered satisfactory. Simulation results and their uncertainties due to model parameters are within the experimental error bars, so that the model can be considered validated on this flame.

3.2. Coflow laminar diffusion flame

Motivated by the promising results of the 1D flame, a more challenging flame was targeted. The flow and the flame structure of coflow non-premixed cases are more complex than the ones from premixed flames such as the ISF-premixed-laminar-3 flame. Though the increased use of TiRe-LII for experimental d_{pp} determination, a limited number of measurements can be found for laminar diffusion flames. To explore the validity of the primary particle model on such a flame, the ISF-coflow-laminar-3 flame was a proper choice, because several experimental results are available. In addition, for this kind of flame, the formation processes of mature soot particles like aggregation are more relevant (soot particles up to $d_{pp} = 70$ nm were observed with TEM [78] at high equivalence ratio) allowing for a complementary validation of the post-processing procedure compared to the results of Section 3.1.

The burner (YDB) was originally designed at Yale University [79,80] and shared with other laboratories. The simulation results are compared below with the experimental results obtained at the EM2C Laboratory [81] and at the University of Adeilade [78]. Here, only a brief overview of the configuration is given, while a detailed description can be found in the above-referred papers.

Ethylene-nitrogen mixture and air were injected through two co-axial tubes with an internal diameter of 3.9 mm (0.38 mm wall thickness) and of 50 mm, respectively. The bulk velocity was 35 cm/s for both inlets. A uniform inlet profile was ensured with a honeycomb mesh at the airflow side. The fuel side is usually assumed to have a fully developed, parabolic velocity profile generally developed in tubes. The measurements were carried out with four different dilutions for the fuel stream: 32% (F32), 40% (F40), 60% (F60) and 80% (F80) ethylene content respect to the volume. The validation is here performed on the richest flame, which is the most challenging operating condition due to the presence of big aggregates. Results on d_{pp} for the other ethylene contents will be presented in Section 4, whereas the soot volume fraction results are provided as Supplementary material.

3.2.1. Numerical setup

The simulations were performed with the laminarSMOKE code [61], which operates in the framework of OpenFOAM and was specifically designed to solve multidimensional laminar reacting flows with detailed kinetic mechanisms. The classical conservation equations – mass, momentum, energy and species – for continuous, multicomponent, compressible, thermally-perfect mixtures of gases (including the chemical source terms) were solved. Measurements showed that particle size does not exceed 1 µm, therefore, particles can be assumed to follow the gas flow in the current laminar diffusion flames [82].

The thermophoretic and Soret effects were accounted for in the simulation and the buoyancy effect was considered. The flow field was calculated with a SIMPLE solver [83,84] and a second order centered spatial discretization scheme was applied.

The simulation domain was simplified to two dimensions as a result of the axial symmetry of the problem. The structured numerical mesh of size 15×7 cm (height $\times$ radial extent) accounts for 3600 cells in case of the coarse mesh (80×45, $\Delta x \approx 0.3$ mm and $\Delta y \approx 1$ mm in the flame region) and 41,600 cells for the fine mesh (400×104, $\Delta x \approx 0.15$ mm and $\Delta y \approx 0.2$ mm in the flame region), both with increased resolution in the flame region. The extent of the mesh ensured that the boundary conditions do not affect the flame region. Due to the intense computational demand of the high-resolution mesh, the simulations with the finer mesh were carried out only for F32 and F80.

Dirichlet conditions were imposed to fix the velocity, the temperature and the composition on the inlet. At the fuel inlet (inner stream) a fully developed, parabolic velocity profile was assumed. A uniform flow profile was imposed for the oxidizer (outer) stream. The streams were injected with a bulk velocity of 35 cm/s, atmospheric pressure and 293 K temperature. Neumann conditions were adopted to model the outflow at the top of the computational domain. At the centerline, symmetry conditions were imposed.

3.2.2. Results

In the following section, the flame with 80% volumetric ethylene content in the fuel stream is investigated. The soot volume fraction is compared to the measurement results found in the literature.

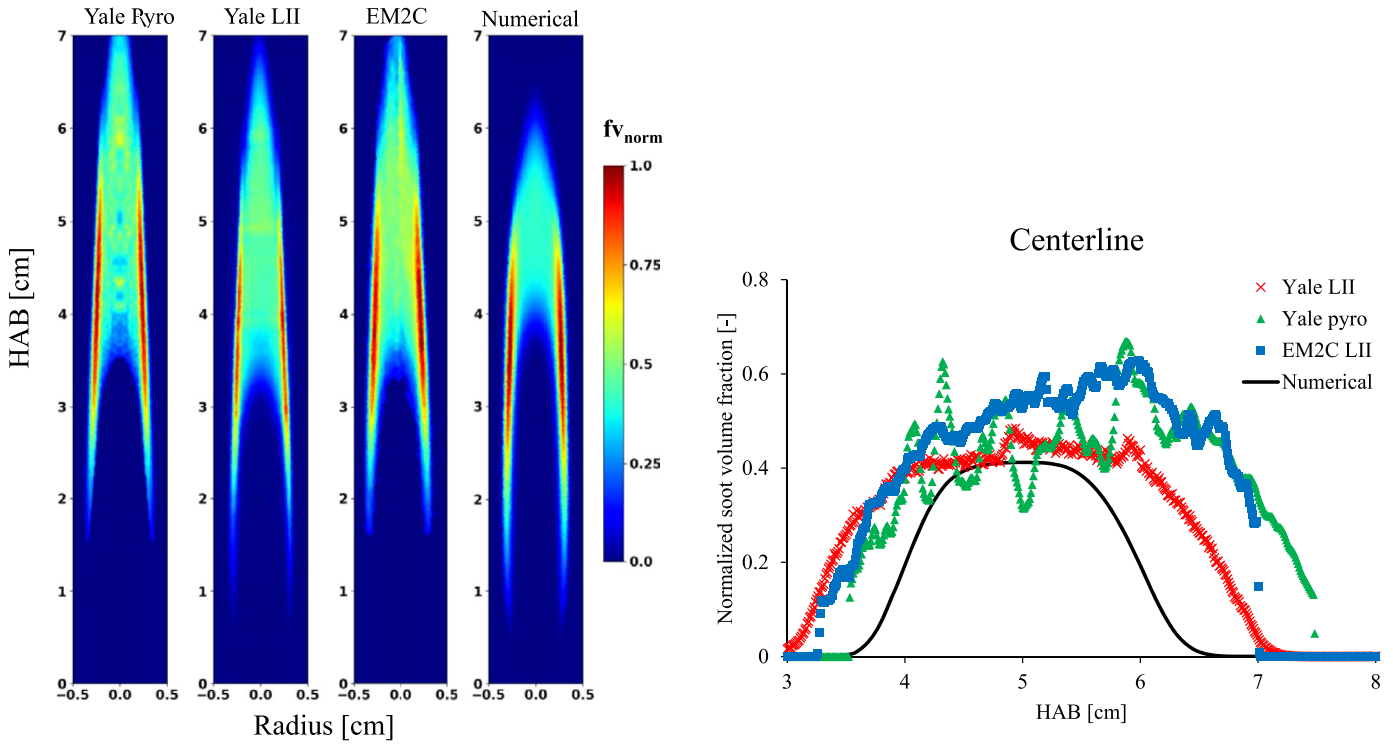

Fig. 6. ISF-coflow-laminar-3 F80: comparison of normalized soot volume fraction in the whole flame cross-section (left) and the along centerline (right) between measurements [81,85,86] and simulation.

Table 1
ISF-coflow-laminar-3 F80: Soot volume fraction peak values in ppm.

Case	Yale Pyro [85]	Yale LII [86]	EM2C LII [81]	Numerical
Max f_v	4.0	4.3	4.65	1.67

In Fig. 6 the experimental [81,85,86] and the numerical soot volume fractions normalized by their peak value (values provided in Table 1 for each case) are presented in the flame cross-section and along the centerline. The numerical determination of soot volume fraction was performed using $d_{\mathrm{pp},N_{\mathrm{min}}} = 2$ nm. As for the premixed case, the difference observed when assuming $d_{\mathrm{pp},N_{\mathrm{min}}} = 5$ nm is marginal (less than 1%). The peak value of the experimental soot volume fraction is ~ 3 times higher than the numerical simulation. The simulation predicted faster soot oxidization, which results in a shorter axial sooty region. However, it should be noticed that the transition of the high soot volume fraction region from the center to the wings with decreasing dilution was captured by the numerical simulations (See Fig. 1 of the Supplementary material).

Being able to correctly predict this feature if particularly challenging for a soot model and is rarely verified in literature. Recent models may provide good agreement for one specific coflow flame, but usually obtain a mismatch for other flames [49,50,86–88]. Alternatively, they may capture the peak value for several coflow flames, but without providing the spatial distribution for the varying dilution [89], so that the agreement with experiment cannot be definitely assessed. Furthermore, only a few models have been tested both on premixed flames and coflow flames [41,49]. The herein used kinetic scheme was validated on various premixed flames [56,90–93] and no model parameter adjustment was carried out for the current cases. Despite the underprediction in terms of f_v and length of the centerline sooty region, as the performance is in accordance with the state-of-the-art models, the results will be used to apply the new procedure and evaluate its interest.

Different cases have been considered to estimate the primary particle size for the 80% flame, summarized in Table 2.

First, the impact of the retained definition for the mean d_{pp} is evaluated in cases a-b-c. In addition the effect of the low cut-off size on the d_{pp} results can be evaluated by comparing case d to case a. It should be noticed that the variability introduced by the definition for the calculation of the mean diameter and the choice of $d_{\mathrm{pp},N_{\mathrm{min}}}$ is not due to the proposed post-processing procedure, but it is related to the general issue of correctly comparing experimental and numerical results. Results for these four cases are presented in Fig. 7 and it can be observed that the variability can be important and it has to be taken into account to perform a consistent validation of the numerical results.

Similarly to the 1D case, the monodisperse diameter (case b) is the largest, followed by the arithmetic mean diameter (case c) and by the count mean diameter (case a). The characteristics of the spatial distribution are very similar: the highest values are located on the wings, rapidly increasing between ~ 1 and ~ 2.5 cm HAB, while decreasing from ~ 4 to ~ 5 cm HAB. Along the centerline, after a rapid increase, a plateau of mean d_{pp} appears before oxidation of the particles.

By comparing case (a) to case (d) it is possible to verify that the choice of the low cut-off size may introduce a significant variability for the mean primary particle size, similarly to the 1D case investigated in Section 3.2. By choosing a smaller $d_{\mathrm{pp},N_{\mathrm{min}}}$, the maximum diameter dropped from 22 nm to 17 nm and the whole spatial distribution is modified. In addition, in the inner region, the d_{geom} shifted to lower values when considering $d_{\mathrm{pp},N_{\mathrm{min}}} = 2$ nm. As already stated, the choice of this parameter is mainly governed by the sensitivity of the experimental setup to capture small particles presence. In this case, no information is provided by the authors in [81]. However, where large particles are present, small particles (below 5 nm) are generally not expected to be detected by LII especially for high delay times [76,94]. As the ISF-coflow-laminar-3 series is characterized mainly by a larger mean primary particle

Table 2
ISF-coflow-laminar-3: F80 numerical simulation cases.

Case	Low cut-off size	Prim. Part. model	Surf. rounding	Mean def.	d_{pp,N_s}
a	BIN_8 (5 nm)	post-proc.	active	geom	BIN_{12} (10 nm)
b	BIN_8 (5 nm)	post-proc.	active	mono	BIN_{12} (10 nm)
c	BIN_8 (5 nm)	post-proc.	active	amean	BIN_{12} (10 nm)
d	BIN_5 (2 nm)	post-proc.	active	geom	BIN_{12} (10 nm)
e	BIN_8 (5 nm)	$d_{ag,pp}$ =10 nm	–	geom	BIN_{12} (10 nm)
f	BIN_8 (5 nm)	Vol. equiv. sphere	–	geom	BIN_{12} (10 nm)
g	BIN_8 (5 nm)	post-proc.	inactive	geom	BIN_{12} (10 nm)
h	BIN_8 (5 nm)	post-proc.	active	geom	BIN_{10} (6.4 nm)
i	BIN_8 (5 nm)	post-proc.	active	geom	BIN_{14} (16 nm)

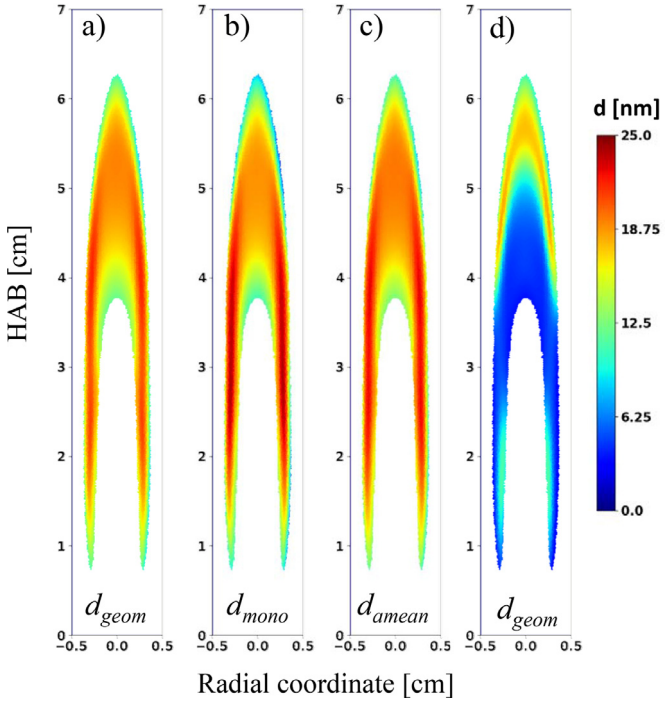

Fig. 7. ISF-coflow-laminar-3: numerically determined d_{geom}, d_{mono} and d_{amean} (cases specified in Table 2).

size compared to the ISF-premixed-laminar flame, it may be reasonable to assume that the contribution of small particles to the LII signal is negligible and then to consider $d_{pp,N_{min}} = 5$ nm. Nevertheless, it is important for future validations to dispose of an indication of the experimental low cut-off size as the whole comparison can be biased by this choice.

In order to evaluate the performances of the newly developed method for tracking mean d_{pp}, the numerical results are compared to the experimental data from Franzelli et al. [81] in Fig. 8. Results obtained using the original mechanisms' description of d_{pp} [56] (case e) and assuming a spherical assumption (case f) are also provided in Fig. 8 to highlight the interest of the proposed technique.

It can be observed that the implemented model (case a and b) gives a better estimation of d_{pp} than the previously applied assumptions. Indeed, the maximum d_{pp} value is correctly localized in the flame wings whereas a lower almost constant value is observed along the flame centerline. On the contrary, for case e the mean d_{pp} value is homogeneously equal to 10 nm. This value corresponds to d_{pp,N_s} proving that in this case, the contribution of small spherical particles to the mean d_{pp} is negligible compared to the aggregates. Though the spherical particle assumption (case f) provides larger maximal d_{geom} as expected, the spatial distribution of d_{geom} is clearly unsatisfactory.

On the contrary, with the new model, a plateau of the d_{pp} value is observed between ~4.5 and ~6.5 cm along the centerline in agreement with the measurements. The d_{pp} on the wings slightly decreases between HAB = ~3.5 and ~5 cm HAB both in the experiments and in the numerical simulation.

To conclude, it has to be observed that the maximum value of d_{pp} is underestimated by a factor of 3 compared to the experimental values obtained by LII [81]. In addition, the contrast between the centerline and the wings is not that significant in the numerical results as in the experiments. However, the dominance of large particles on the wings is correctly captured, leading to a relevant improvement compared to the original CSDM results and to the sphericity assumption.

In addition to the LII measurement data [81], the mean diameters obtained with TEM by Kempema and Long [78] are available at 3 locations on the centerline and 3 locations on the wings. In Fig. 9 the numerical and the experimental mean d_{pp} is compared along the centerline and at the three TEM measurement heights on the wings. As the radial coordinates of the TEM probe locations were not provided, the numerical values are here extracted at maximum d_{pp} location of a given height. The numerical results show a quite good agreement with the TEM data both along the centerline and the wings. It should be reminded that it is well known that TEM and LII techniques do not strictly measure the same quantity and that some discrepancies can be observed among these two approaches [81]. Consequently, it is not possible to discriminate what is the correct experimental database to be used to validate the model. However, it is possible to conclude that the numerical results are in a reasonable agreement compared to the experimental uncertainties.

Sensitivity to model parameters

In order to clarify the relevance of this procedure, it is important to discuss the sensitivity to its parameters. Therefore, as done for the premixed case, the effect of the surface rounding and the value of d_{pp,N_s} on the results is investigated here.

The role of the correction parameter for surface rounding can be determined by comparing case (a) to case (g) (in Fig. 10). Due to the high contribution of condensation and surface growth processes, the correction for surface rounding significantly impacts the primary particle diameter (contrary to the premixed case shown in Section 3.2). When neglecting the surface rounding correction the maximum d_{geom} changes from ~22 to ~18.2 nm. This highlights the different nature of laminar diffusion and premixed flames and the importance of introducing the C_r factor into the model.

The sensitivity to the choice of the smallest aggregating particle size, d_{pp,N_s}, was also tested. The variation of the d_{geom} is depicted in Fig. 10. By modifying d_{pp,N_s} to 6.4 nm (case h) and 16 nm (case i), from the baseline 10 nm (case a), the values of d_{geom} are slightly modified. However, the characteristics of the spatial profile are unchanged.

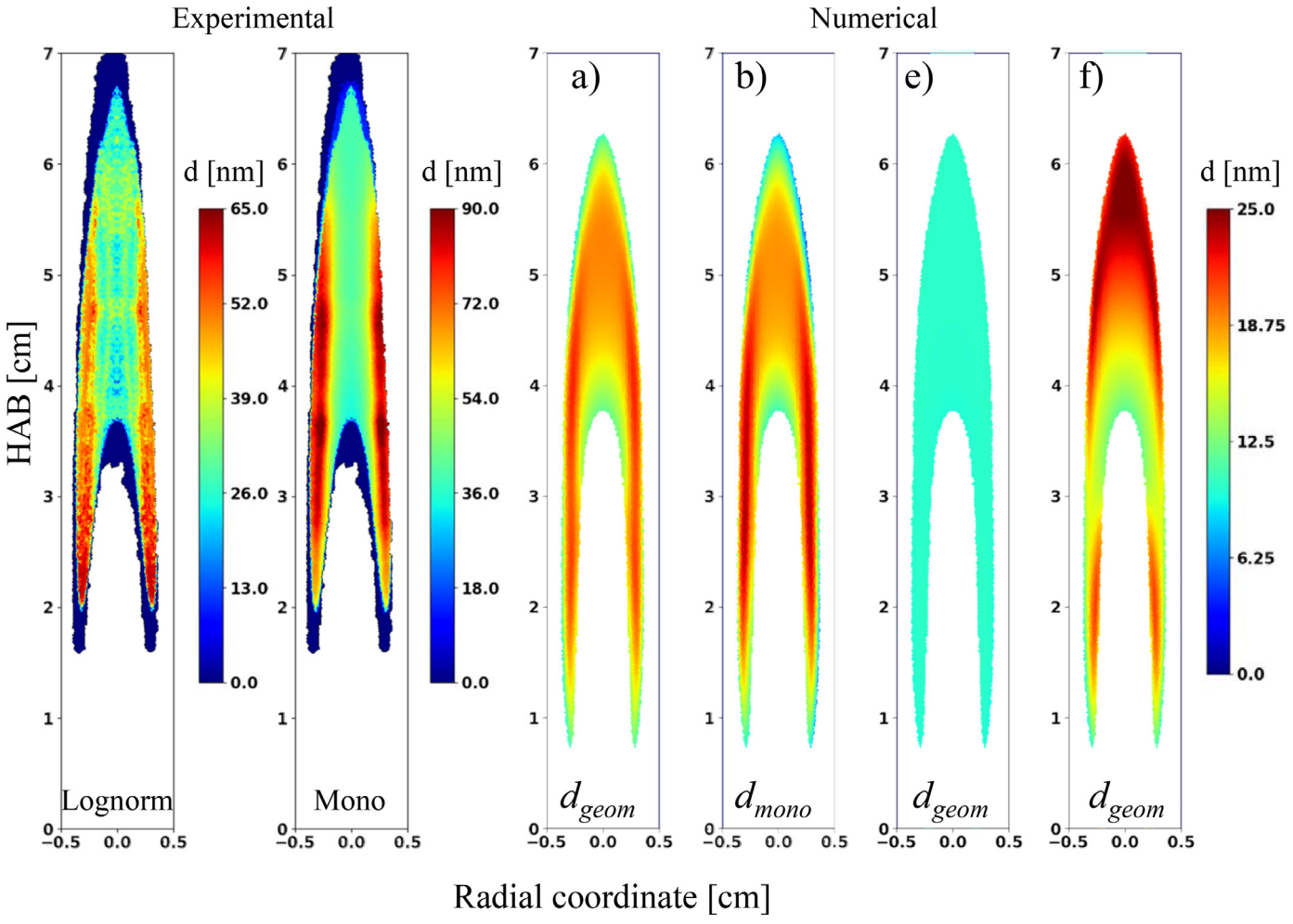

Fig. 8. Experimental results [81] on d_{pp} compared to the numerical results using the new strategy (cases a and b), assuming aggregates with constant d_{pp} (case e) and spherical particles assumption (case f) in F80.

Overall, it can be concluded that even if the quantitative d_{pp} values may depend on the model parameters and improvements of the CSDM description are still needed, the interest of the proposed tracking procedure is clearly proven since it allows to recover the spatial trend of d_{pp}, greatly improving the original description. In addition, since relevant differences are detected between the newly predicted d_{pp} values and the ones obtained with the original CDSM assumption, accounting for the coupling of the soot reaction kinetics with d_{pp} information may modify the prediction on f_v and represents a possible future improvement of the CRECK Modeling Group's detailed model.

In the following, this technique is applied to the investigation of the dilution effects on the spatial distribution of d_{pp} in the YDB flame series.

4. Dilution effects on the mean primary particle diameter

The four reference dilution values (32%, 40%, 60%, and 80% of ethylene in the fuel mixture), experimentally characterized in [81], are considered here. Both experimental and numerical results of the d_{geom} are represented in Fig. 11. Similarly to the 80% case, the quantitative values of d_{geom} are underestimated by a factor of 3–5 compared to experiments for all the flames. Based on the difference between TEM and LII results, between different LII results (a factor of 3 has been observed when comparing d_{mono} from Franzelli et al. [81] and Foo et al. [95] for the F32 case) and the numerical errors previously discussed, only a qualitative comparison is attempted here.

In terms of d_{pp} trends, the experimental behavior is correctly reproduced: a nearly homogeneous value of d_{geom} is retrieved for the 32% and the 40% cases, whereas the 60% and the 80% cases are characterized by the presence of big particles localized in the flame wings. It should be noticed that a better agreement with experiments is expected by improving the kinetic mechanism prediction on f_v and by coupling the d_{pp} information to the reaction rates calculation. However, the main characteristics are well reproduced and the conclusions of the base evaluation are not expected to change significantly.

In the experimental work [81], it was inferred that the observed increase of f_v and d_{pp} levels in the flame wings with fuel presence in the diluted mixture was due to two different phenomena: the increase of precursors concentrations and the change in the flame temperature. To validate (or not) the experimental conclusions, the temperature, the heavy PAH concentration and the soot formation rate are investigated for F32 and F80 in Fig. 12. The flame temperature is presented in Fig. 12a, together with isolines of 10% of the maximum rate for nucleation,[2] mass growth,[3] and oxidation to localize the different soot reaction zones. The field

[2] Chemical reactions $BIN_i => BIN_j$ $i \leq 4$ and $j \geq 5$.

[3] Sum of surface growth by condensation of PAH, heavy PAH and resonance stabilized radicals, and the HACA-mechanism [56].

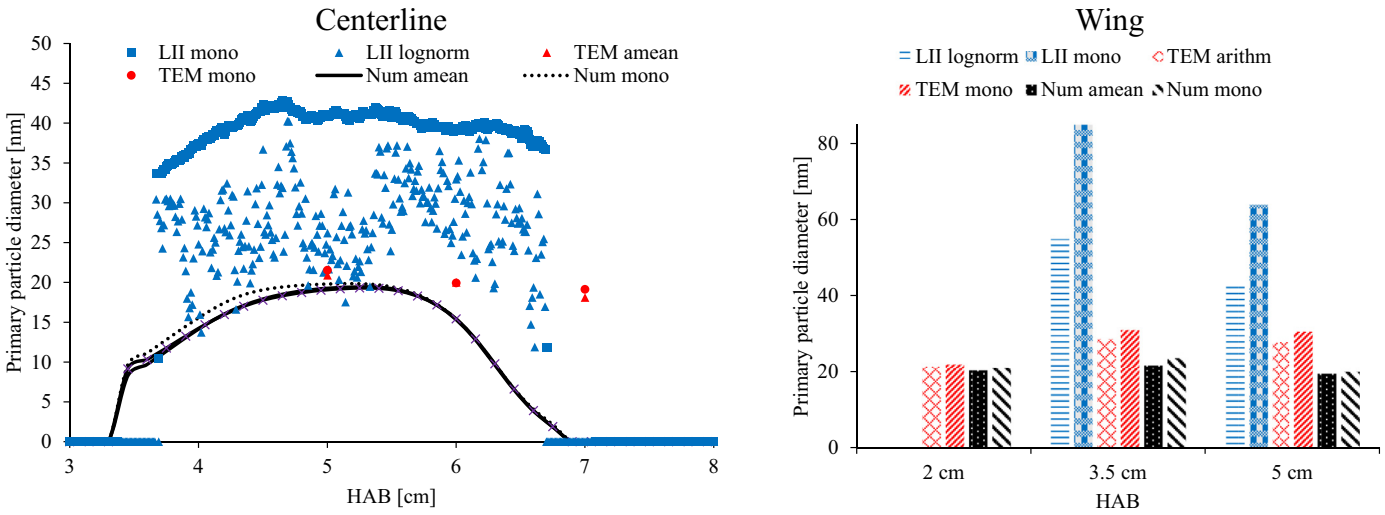

Fig. 9. d_{pp} along the centerline and at three HAB on the wing for ISF-coflow-laminar-3. Comparison of numerical results to LII results [81] and TEM data [78].

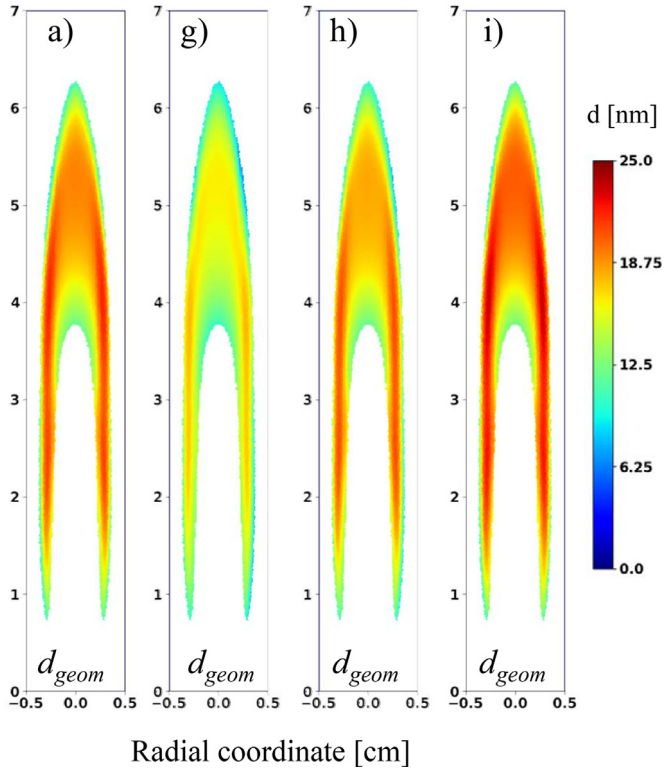

Fig. 10. Numerical d_{pp} results using the new strategy with different model parameters in F80.

of heavy PAH (BIN_1-BIN_5) concentration is plotted in Fig. 12b, whereas the soot inception rate and the total mass growth rate are presented in Fig. 12c.

By looking at the nucleation and growth regions in Fig. 12a, it can be noticed that in both situations the soot mass production does not occur in the high-temperature region, so that the increase of the maximum temperature value does not seem to directly affect soot production and, consequently, the primary particle diameter size. On the contrary, soot production seems to be localized in a region where $T \approx 1800$ K, whose extension increases with the ethylene content in the mixture, leading to a higher total soot production but not necessarily to a higher local peak of production in the flame wings.

By looking at Fig. 12b, it can be observed that the concentration of soot precursors increases with the ethylene content. The formation rates significantly intensify downstream of the high heavy PAH concentration region, which may indicate the connection between increased ethylene content, increased precursor concentration, intensified growth process and finally higher soot formation and d_{pp}. However, it should be noticed that the maximum of PAH concentration and growth rate is localized in the centerline also for F80, despite the maximum of d_{pp} is observed on the wings. Therefore, the increase of temperature and PAH concentration does not seem to be directly responsible for an increase of d_{pp} in the flame wings.

To understand the presence of the maximum mean d_{pp} value in the flame wings for the F80 case, it should be reminded that the d_{pp} depends not only on the local rates of the formation processes but also on the residence time of the fluid parcel in the growth and nucleation area. In analogy, the particle history will also affect the size of its primary particles. In Fig. 13, the rate of growth processes and the d_{geom} are plotted as a function of the residence time along the centerline for both the F32 (red) and the F80 (black). The link between HAB and residence time is indicated in Fig. 13b. Along the centerline, both nucleation and growth show a profile consisting of a single peak. It can be observed that the formation of larger primary particles in the centerline for the F80 case is on the one hand due to the increased intensity of the growth process and on the other hand due to the increased time spent by the particles in the region of growth processes.

In addition, to investigate the flame wings, a streamline has been chosen in a way that it passes through the location of the maximum d_{geom} for the F80 flame. The evaluation performed along this streamline is presented in Fig. 13 in green. The scenario at the wings is more complex than the one from the centerline: nucleation and growth processes overlap for a long period and their shape deviates significantly from the trend along the centerline. Even if the peak of growth rate is similar along the centerline and the wings, the time spent by the particle in the wings is longer compared to the centerline so that bigger primary particles are formed.

By looking to results of Fig. 13b., it can be observed that, along the wings of F80, the d_{geom} strongly increases where the contribution of growth processes are significantly higher than soot inception. Then, between 20 and 25 ms residence time (HAB = 2.8–3.5 cm) the mean d_{pp} value slightly reduces with the HAB, before

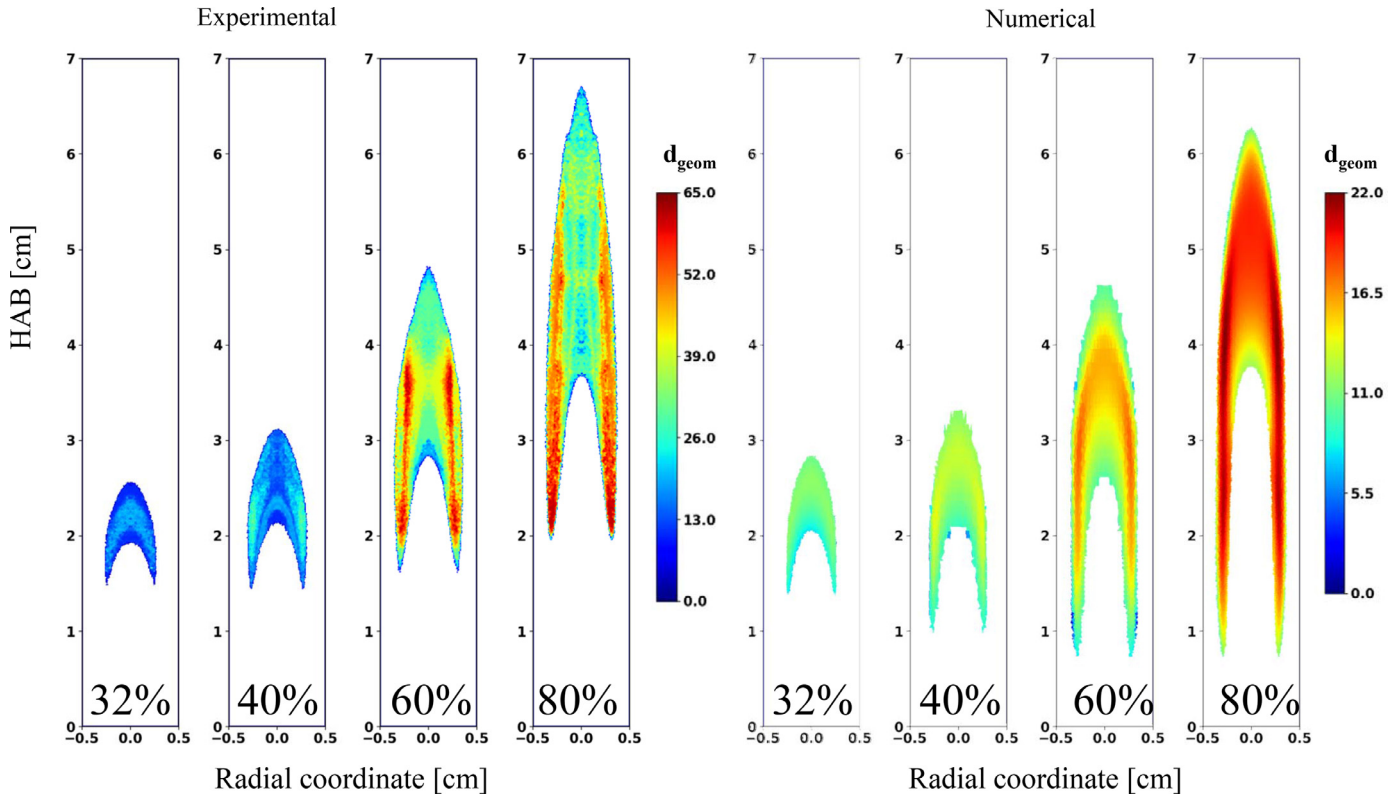

Fig. 11. Experimental [81] and numerical mean primary particle diameters (d_{geom}) for four dilutions. (For interpretation of the references to color in this figure legend, the reader is referred to the web version of this article.)

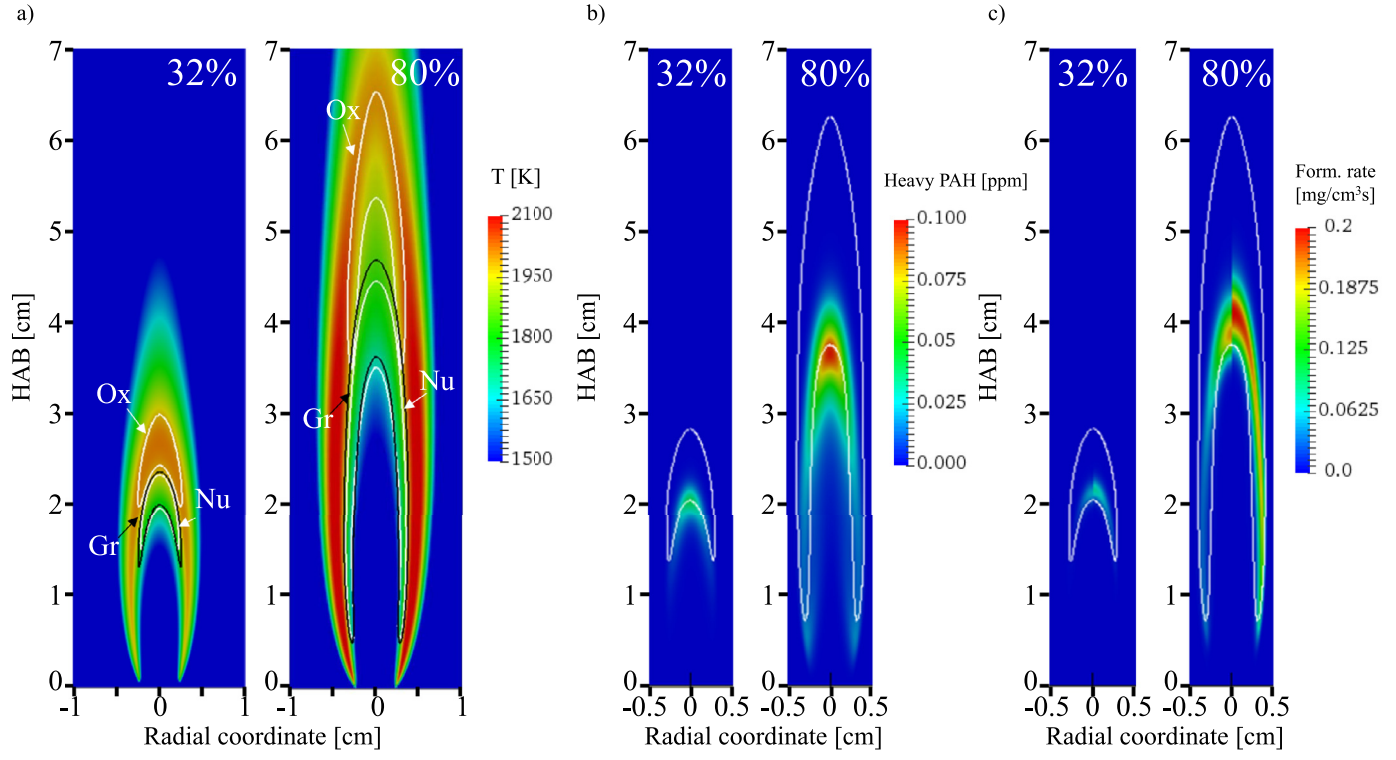

Fig. 12. (a) Isolines of nucleation (Nu-white), growth processes (Gr-black) and oxidation (Ox-white) rate reaching 10% of the maximum value with temperature distribution,(b) heavy PAH (BIN_1-BIN_5) concentrations with isoline $f_v = 0.01$ ppm and(c) soot inception (left) and growth process rates (right) with isoline $f_v = 0.01$ ppm in the F32 and F80 flames. (For interpretation of the references to color in this figure legend, the reader is referred to the web version of this article.)

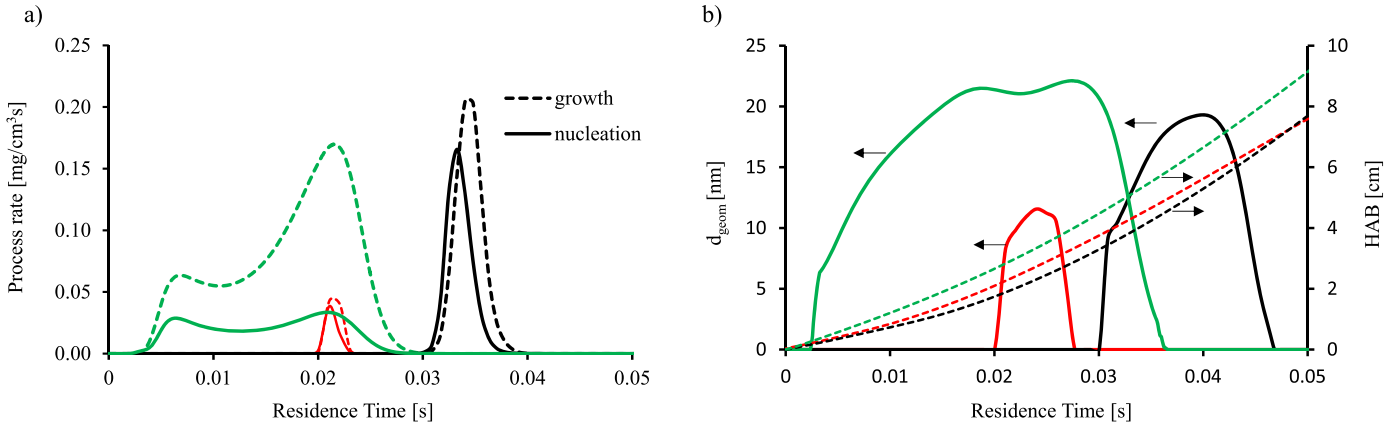

Fig. 13. (a) nucleation and growth intensity (b) d_{geom} and HAB along centerline for F32 (red) and F80 (black) and streamline crossing maximum d_{geom} location for F80 (green). (For interpretation of the references to color in this figure legend, the reader is referred to the web version of this article.)

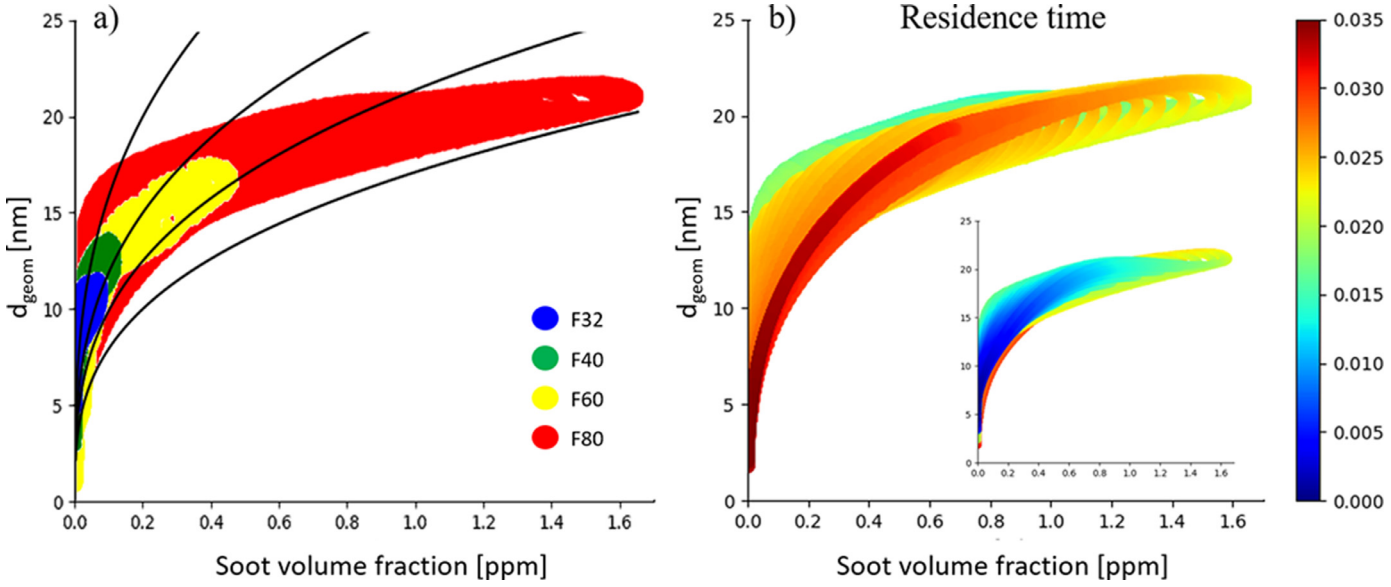

Fig. 14. (a) d_{geom} and f_v correlation for all ISF-coflow-laminar-3 flames. Black lines indicate 3rd root relation between d_{geom} and f_v. (b) d_{geom} and f_v correlation in F80 flame colored by residence time [s]. (For interpretation of the references to color in this figure, the reader is referred to the web version of this article.)

the intense oxidation of the soot begins. In this 'plateau' region the soot volume fraction is still increasing (Fig. 6) but the mean d_{pp} value is almost constant due to the intense production of small particles that attenuates the effects of growth processes. The observed behavior is slightly in contradictions with the conclusions of Franzelli et al. [81] inferring a positive correlation between primary particle size and soot volume fraction.

In order to characterize the relation between d_{geom} and f_v, the numerical results for the four coflow flames are presented in Fig. 14. The black lines indicate the 3rd root relation between d_{geom} and f_v. Assuming a monodisperse distribution, these lines correspond to a f_v growth for a constant total primary particle density ($\rho_{pp,tot}$). This feature occurs when nucleation and coagulation are negligible and surface growth and condensation are the main processes. A positive correlation between the two variables is observed in agreement with the one inferred by Franzelli et al. [81].

When decreasing the fuel dilution, the values of both the largest d_{geom} and the largest f_v increase, but the regions for F32, F40 and F60 mainly overlap. For small soot volume fraction, the d_{geom} greatly increases following the 3rd root relation, indicating that it is the results of surface growth and condensation processes. In the F80 case, different $\{d_{geom}, f_v\}$ pairs appear even for small f_v values compared to the other three cases. The oxidation of the large and numerous aggregates results in small primary particles. However, they still represent a significant amount of soot volume fraction resulting in a low d_{geom} for $f_v < 0.4$ ppm in the higher ethylene content flames.

In order to understand the origin of the new ranges, let us first recall the effect of the soot related processes. The coalescence increases the diameter, while f_v remains constant. The oxidation decreases both the diameter and f_v, however, as small particles oxidate faster and may be completely consumed, it may lead to a possible overall increase of d_{geom}. The inception increases the f_v, while the mean diameter is decreasing towards the nuclei size. The growth processes increase both the mean diameter and f_v. As highlighted earlier, not only the rate of the process, but also the residence time in the different regions is important. In Fig. 14b the residence time is presented. $d_{geom} = 20$ nm is reached in less than 15 ms and the further increase of residence time is not resulting in significantly larger d_{geom} but in f_v increment. It can be observed that d_{geom} is not strictly related to the residence time in general. This is related to the fact that the residence time in the active re-

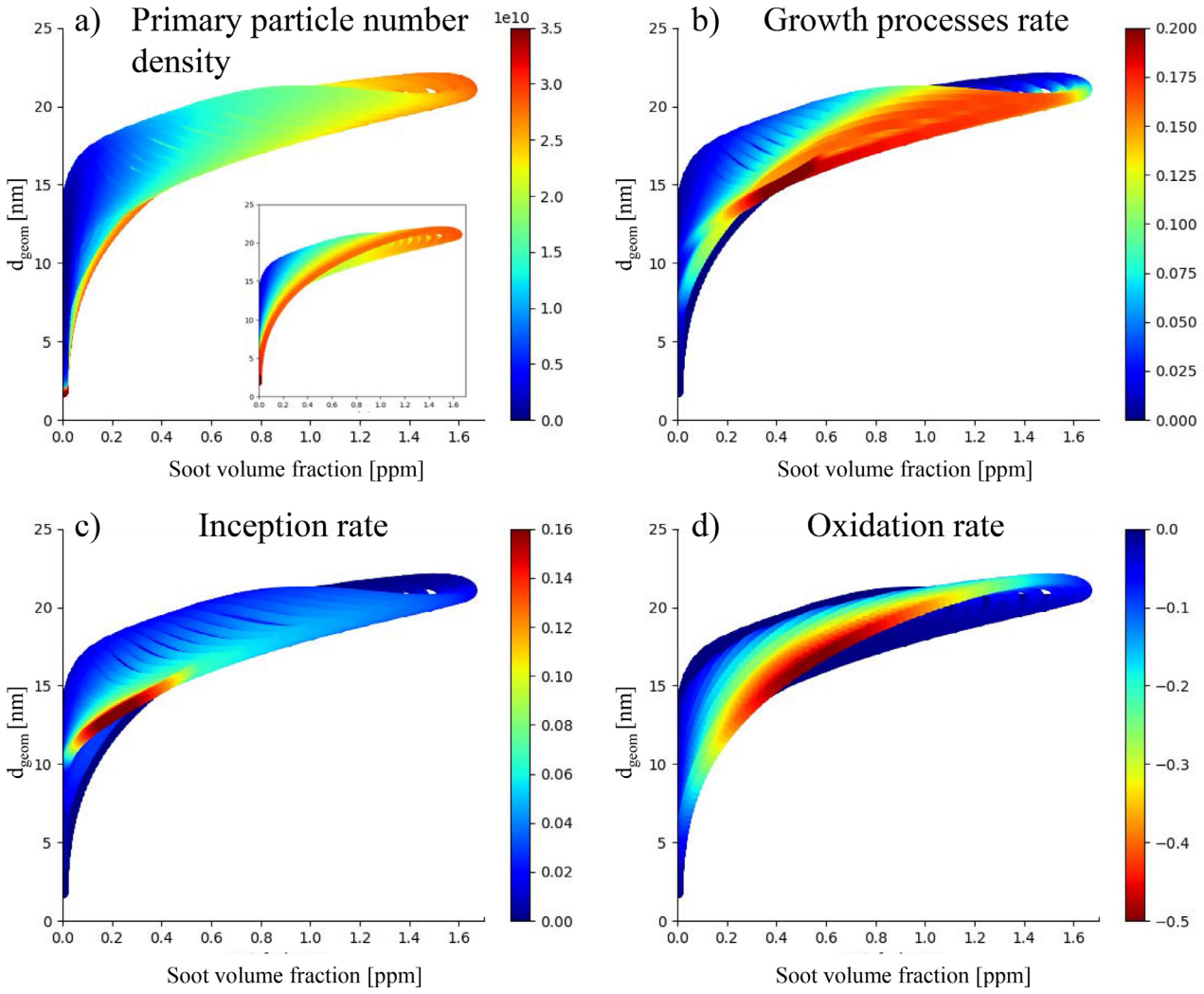

Fig. 15. d_{geom} and f_v correlation in F80 flame colored by (a) the total primary particle number density [#/cm^3] and by the rate of (b) Growth process (b) Inception and (d) Oxidation [mg/cm^{3}s]. (For interpretation of the references to color in this figure legend, the reader is referred to the web version of this article.)

gions of the soot formation processes are crucial. The total primary particle number and the process rates of inception, growth processes, and oxidation are presented in Fig. 15.

For small f_v, large d_{geom} values can be reached through coalescence. The $\rho_{pp,tot}$ remains almost constant while larger d_{geom} is reached, which indicates that the inception and the coalescence cancel each other's effect on $\rho_{pp,tot}$. The large f_v region coincides with the high growth process intensity, however, between $\sim$0.8 and $\sim$1.4 ppm the growth processes do not lead to larger d_{geom} around $\sim$20 nm. This can be explained by the fact that an increase of primary particle number density caused by inception is observed, which overcomes the effect on d_{geom} by the growth processes and the coalescence. The largest d_{geom} is reached where the oxidation, the growth processes, and the inception are present. Since d_{geom} is dependent on the shape of the PPSD, the combination of the various processes can result in a d_{geom} increment. These observations indicate that despite a general positive correlation between f_v and d_{geom} the primary particle size may vary in a limited range for the various f_v values.

From the discussed analysis, it can be concluded that the effect of dilution on the transition of d_{pp} peak values from the centerline to the flame wings cannot be linked in a straightforward manner to an increase of temperature and precursor concentration. The contribution rate and location of the different formation and destruction processes to the soot particle evolution changes with the increase of ethylene content. This is not only due to differences in the flame structure but also in the streams' physical properties, in particular, the velocity field governing the trajectory of the particles and, consequently, their residence time in growth regions.

5. Conclusions

Currently available chemical discrete sectional models (CDSMs) do not provide information about the primary particle size. In this work, a general primary particle post-processing method was proposed for CDSMs. The performance of the model combined with the kinetic mechanism of the CRECK Modeling Group [56] was tested on ISF target flames [60]: a premixed laminar ethylene flame [69] and a coflow diffusion ethylene flame series [80] with various dilutions. The model included a correction for the surface rounding, which turned out to play a significant role in the coflow diffusion flames where surface growth is more intense.

The sensitivity to the low cut-off limit used to calculate the mean diameter was investigated. The influence of the change from 2 nm to 5 nm was significant, which suggests to have a careful

look at the smallest detected primary particle size of the measurements while validating the numerical results.

The soot volume fraction was well predicted for the ISF-premixed-laminar-3 flame (within the uncertainty limits) and the numerically obtained mean primary particle size showed good agreement with the experimental results [67–69].

For the ISF-coflow-laminar-3 flame the soot volume fraction was underpredicted by a factor of $\sim$3 to 4 for all four dilutions. Similarly, the d_{pp} values are smaller than the LII experimental data [81] by a factor of 2–4, and slightly smaller than the TEM results [78] indicating that improvements of the CDSM are needed.

However, it has been observed that the mean d_{pp} determined with the new method is providing a qualitative agreement for all dilutions compared to the results obtained with the typical assumptions of CDSMs, i.e. assuming spherical aggregates or constant primary particle size for all aggregates.

Having access to a detailed description of the soot production processes, the effect of dilution on the localization and the level of mean primary particle diameter has been discussed. In particular, it has been shown that the residence time plays an important role in the localization of primary particle diameter. Finally, it has been proven that the positive correlation between primary particle size and soot mass fraction inferred by Franzelli et al. [81] is globally observed, but it is not strictly verified. In the upper part of the wings of the F80 flame the intense nucleation results in a decreasing mean primary particle size despite the soot volume fraction is still increasing. Furthermore, at low soot volume fractions, the mean diameter might increase without a significant soot volume increment due to inception and subsequent coalescence.

Overall the new method was shown to be a promising tool for evaluating primary particle size in numerical simulation of flames where CDSM is applied. A better understanding of particle formation was possible with combining the knowledge gained about the soot processes by using the CDSM and the primary particle number tracking.

As future work, in order to improve the performance of the kinetic mechanism, the coupling between the predicted primary particle size and the chemical reaction coefficients should be implemented. Combining the proposed primary particle analysis with other kinetic mechanisms might be also a target of interest.

Acknowledgments

This project has received funding from the European Union's Horizon 2020 research and innovation program under the Marie Sklodowska-Curie grant agreement No. 643134.

M. Roussillo and P. Scouflaire (EM2C Laboratory, CNRS/CentraleSupélec) are acknowledged for providing the experimental results. Warumporn Pejpichestakul (CRECK Modeling Group, Politecnico di Milano) is acknowledged for her help regarding the kinetic mechanism. Authors would like to thank K.K. Foo (Univerity of Adeilade) for providing the experimental data and for the personal communication. B. Franzelli acknowledges the support of the European Research Council (ERC) under the European Unions' Horizon 2020 research and innovation programme (grant agreement No. 757912).

Supplementary material

Supplementary material associated with this article can be found, in the online version, at doi:10.1016/j.combustflame.2019.06.008.

References

[1] S. Jose, K. Niranjan, B. Gharai, P.V.N. Rao, V.S. Nair, Characterisation of absorbing aerosols using ground and satellite data at an urban location, Hyderabad, Aerosol Air Qual. Res. 16 (6) (2016) 1427–1440, doi:10.4209/aaqr.2014.09.0220.
[2] J. Hansen, L. Nazarenko, Soot climate forcing via snow and ice albedos, Proc. Natl. Acad. Sci. 101 (2004) 423–428, doi:10.1073/pnas.2237157100.
[3] U. Pöschl, Atmospheric aerosols: composition, transformation, climate and health effects, Angew. Chem. – Int. Ed. 44 (2005) 7520–7540, doi:10.1002/anie.200501122.
[4] M. Shiraiwa, K. Selzle, U. Pöschl, Hazardous components and health effects of atmospheric aerosol particles: reactive oxygen species, soot, polycyclic aromatic compounds and allergenic proteins, Free Radic. Res. 46 (2012) 927–939, doi:10.3109/10715762.2012.663084.
[5] C.M. Sorensen, G.D. Feke, The morphology of macroscopic soot, Aerosol Sci. Technol. 25 (1996) 328–337, doi:10.1080/02786829608965399.
[6] J. Lahaye, Particulate carbon from the gas phase, Carbon 30 (1992) 309–314, doi:10.1016/0008-6223(92)90025-R.
[7] U. Koeylue, Y. Xing, D.E. Rosner, Fractal morphology analysis of combustion-generated aggregates using angular light scattering and electron microscope images, Langmuir 11 (1995) 4848–4854, doi:10.1021/la00012a043.
[8] T.L. Barone, J.M. Storey, A.D. Youngquist, J.P. Szybist, An analysis of direct-injection spark-ignition (DISI) soot morphology, Atmos. Environ. 49 (2012) 268–274, doi:10.1016/j.atmosenv.2011.11.047.
[9] M.J. Hounslow, A discretized population balance for continuous systems at steady state, AIChE J. 36 (1990) 106–116, doi:10.1002/aic.690360113.
[10] J.D. Landgrebe, S.E. Pratsinis, A discrete-sectional model for particulate production by gas-phase chemical reaction and aerosol coagulation in the free-molecular regime, J. Colloid Interface Sci. 139 (1990) 63–86, doi:10.1016/0021-9797(90)90445-T.
[11] M. Frenklach, Method of moments with interpolative closure, Chem. Eng. Sci. 57 (2002) 2229–2239, doi:10.1016/S0009-2509(02)00113-6.
[12] B. Zhao, Z. Yang, M.V. Johnston, H. Wang, A.S. Wexler, M. Balthasar, M. Kraft, Measurement and numerical simulation of soot particle size distribution functions in a laminar premixed ethylene-oxygen-argon flame, Combust. Flame 133 (2003) 173–188, doi:10.1016/S0010-2180(02)00574-6.
[13] H. Richter, S. Granata, W.H. Green, J.B. Howard, Detailed modeling of PAH and soot formation in a laminar premixed benzene/oxygen/argon low-pressure flame, Proc. Combust. Inst. 30 (2005) 1397–1404, doi:10.1016/j.proci.2004.08.088.
[14] J.Z. Wen, M.J. Thomson, M.F. Lightstone, S.N. Rogak, Detailed kinetic modeling of carbonaceous nanoparticle inception and surface growth during the pyrolysis of C_6H_6 behind shock waves, Energy Fuels 20 (2) (2006) 547–559, doi:10.1021/ef050081q.
[15] M. Strumendo, H. Arastoopour, Solution of PBE by MOM in finite size domains, Chem. Eng. Sci. 63 (2008) 2624–2640, doi:10.1016/j.ces.2008.02.010.
[16] P. Mitchell, M. Frenklach, Monte Carlo simulation of soot aggregation with simultaneous surface growth – why primary particles appear spherical, Symp. (Int.) Combust. 27 (1) (1998) 1507–1514, doi:10.1016/S0082-0784(98)80558-4.
[17] P. Mitchell, M. Frenklach, Particle aggregation with simultaneous surface growth, Phys. Rev. E – Stat. Phys. Plasmas Fluids Relat. Interdiscip. Top. 67 (6) (2003) 11, doi:10.1103/PhysRevE.67.061407.
[18] M. Balthasar, M. Frenklach, Monte-Carlo simulation of soot particle coagulation and aggregation: the effect of a realistic size distribution, Proc. Combust. Inst. 30 (2005) 1467–1474, doi:10.1016/j.proci.2004.07.035.
[19] N. Morgan, M. Kraft, M. Balthasar, D. Wong, M. Frenklach, P. Mitchell, Numerical simulations of soot aggregation in premixed laminar flames, Proc. Combust. Inst. 31 I (2007) 693–700, doi:10.1016/j.proci.2006.08.021.
[20] J. Etheridge, S. Mosbach, M. Kraft, H. Wu, N. Collings, Modelling soot formation in a DISI engine, Proc. Combust. Inst. 33 (2) (2011) 3159–3167, doi:10.1016/j.proci.2010.07.039.
[21] M. Balthasar, M. Kraft, A stochastic approach to calculate the particle size distribution function of soot particles in laminar premixed flames, Combust. Flame 133 (2003) 289–298, doi:10.1016/S0010-2180(03)00003-8.
[22] S. Salenbauch, A. Cuoci, A. Frassoldati, C. Saggese, T. Faravelli, C. Hasse, Modeling soot formation in premixed flames using an extended conditional quadrature method of moments, Combust. Flame 162 (2015) 2529–2543, doi:10.1016/j.combustflame.2015.03.002.
[23] D. Hou, C.S. Lindberg, M.Y. Manuputty, X. You, M. Kraft, Modelling soot formation in a benchmark ethylene stagnation flame with a new detailed population balance model, Combust. Flame 203 (2019) 56–71, doi:10.1016/J.COMBUSTFLAME.2019.01.035.
[24] M. Frenklach, S.J. Harris, Aerosol dynamics modeling using the method of moments, J. Colloid Interface Sci. 118 (1987) 252–261, doi:10.1016/0021-9797(87)90454-1.
[25] M.E. Mueller, G. Blanquart, H. Pitsch, A joint volume-surface model of soot aggregation with the method of moments, Proc. Combust. Inst. 32 I (2009a) 785–792, doi:10.1016/j.proci.2008.06.207.
[26] M.E. Mueller, G. Blanquart, H. Pitsch, Hybrid method of moments for modeling soot formation and growth, Combust. Flame 156 (2009b) 1143–1155, doi:10.1016/j.combustflame.2009.01.025.
[27] C. Yuan, R.O. Fox, Conditional quadrature method of moments for kinetic equations, J. Comput. Phys. 230 (22) (2011) 8216–8246, doi:10.1016/j.jcp.2011.07.020.

[28] C. Yuan, F. Laurent, R.O. Fox, An extended quadrature method of moments for population balance equations, J. Aerosol Sci. 51 (2012) 1–23, doi:10.1016/j.jaerosci.2012.04.003.

[29] G. Blanquart, H. Pitsch, Analyzing the effects of temperature on soot formation with a joint volume-surface-hydrogen model, Combust. Flame 156 (8) (2009) 1614–1626, doi:10.1016/j.combustflame.2009.04.010.

[30] M.E. Mueller, G. Blanquart, H. Pitsch, Modeling the oxidation-induced fragmentation of soot aggregates in laminar flames, Proc. Combust. Inst. 33 (1) (2011) 667–674, doi:10.1016/j.proci.2010.06.036.

[31] Y. Xuan, G. Blanquart, Effects of aromatic chemistry-turbulence interactions on soot formation in a turbulent non-premixed flame, Proc. Combust. Inst. 35 (2) (2015) 1911–1919, doi:10.1016/j.proci.2014.06.138.

[32] S. Adhikari, A. Sayre, A.J. Chandy, A hybrid Newton/time integration approach coupled to soot moment methods for modeling soot formation and growth in perfectly-stirred reactors, Combust. Sci. Technol. 188 (8) (2016) 1262–1282, doi:10.1080/00102202.2016.1177035.

[33] S. Deng, M.E. Mueller, Q.N. Chan, N.H. Qamar, B.B. Dally, Z.T. Alwahabi, G.J. Nathan, Hydrodynamic and chemical effects of hydrogen addition on soot evolution in turbulent nonpremixed bluff body ethylene flames, Proc. Combust. Inst. 36 (1) (2017) 807–814, doi:10.1016/j.proci.2016.09.004.

[34] S.T. Chong, V. Raman, M.E. Mueller, H.G. Im, The role of recirculation zones in soot formation in aircraft combustors, Combustion, Fuels, and Emissions, 4B, ASME (2018), doi:10.1115/GT2018-76217. V04BT04A008.

[35] A. Wick, F. Priesack, H. Pitsch, Large-eddy simulation and detailed modeling of soot evolution in a model aero engine combustor, Proc. ASME Turbo Expo 4A-2017 (2017) 1–10, doi:10.1115/GT201763293.

[36] G. Blanquart, H. Pitsch, A joint volume-surface-hydrogen multi-variate model for soot formation, Combust. Gener. Fine Carbonaceous Part. (2009) 1–4. 978-3-86644-441-6

[37] Y. Xuan, G. Blanquart, Two-dimensional flow effects on soot formation in laminar premixed flames, Combust. Flame 166 (2016) 113–124, doi:10.1016/j.combustflame.2016.01.007.

[38] S. Salenbauch, M. Sirignano, D.L. Marchisio, M. Pollack, A. D'Anna, C. Hasse, Detailed particle nucleation modeling in a sooting ethylene flame using a Conditional Quadrature Method of Moments (CQMOM), Proc. Combust. Inst. 36 (1) (2017) 771–779, doi:10.1016/j.proci.2016.08.003.

[39] D.L. Marchisio, A.A. Barresi, Investigation of soot formation in turbulent flames with a pseudo-bivariate population balance model, Chem. Eng. Sci. 64 (2) (2009) 294–303, doi:10.1016/j.ces.2008.10.020.

[40] T. Blacha, M. Di Domenico, P. Gerlinger, M. Aigner, Soot predictions in premixed and non-premixed laminar flames using a sectional approach for PAHs and soot, Combust. Flame 159 (2012) 181–193, doi:10.1016/j.combustflame.2011.07.006.

[41] M. Sirignano, J. Kent, A. D'Anna, Modeling formation and oxidation of soot in nonpremixed flames, Energy Fuel 27 (2013) 2303–2315, doi:10.1021/ef400057r.

[42] Q. Zhang, H. Guo, F. Liu, G.J. Smallwood, M.J. Thomson, Implementation of an advanced fixed sectional aerosol dynamics model with soot aggregate formation in a laminar methane/air coflow diffusion flame, Combust. Theory Model. 12 (2008) 621–641, doi:10.1080/13647830801966153.

[43] R.I. Patterson, M. Kraft, Models for the aggregate structure of soot particles, Combust. Flame 151 (2007) 160–172, doi:10.1016/j.combustflame.2007.04.012.

[44] S.H. Park, S.N. Rogak, A novel fixed-sectional model for the formation and growth of aerosol agglomerates, J. Aerosol Sci. 35 (11) (2004) 1385–1404, doi:10.1016/j.jaerosci.2004.05.010.

[45] Q. Zhang, M.J. Thomson, H. Guo, F. Liu, G.J. Smallwood, Modeling of oxidation-driven soot aggregate fragmentation in a laminar coflow diffusion flame, Combust. Sci. Technol. 182 (7) (2010) 491–504, doi:10.1080/00102200903463050.

[46] N.A. Eaves, S.B. Dworkin, M.J. Thomson, The importance of reversibility in modeling soot nucleation and condensation processes, Proc. Combust. Inst. 35 (2) (2015) 1787–1794, doi:10.1016/j.proci.2014.05.036.

[47] N.A. Eaves, Q. Zhang, F. Liu, H. Guo, S.B. Dworkin, M.J. Thomson, CoFlame: a refined and validated numerical algorithm for modeling sooting laminar coflow diffusion flames, Comput. Phys. Commun. 207 (2016) 464–477, doi:10.1016/j.ijpharm.2018.10.071.

[48] S.B. Dworkin, Q. Zhang, M.J. Thomson, N.A. Slavinskaya, U. Riedel, Application of an enhanced PAH growth model to soot formation in a laminar coflow ethylene/air diffusion flame, Combust. Flame 158 (9) (2011) 1682–1695, doi:10.1016/j.combustflame.2011.01.013.

[49] M.R. Kholghy, A. Veshkini, M.J. Thomson, The core-shell internal nanostructure of soot – a criterion to model soot maturity, Carbon 100 (2016) 508–536, doi:10.1016/j.carbon.2016.01.022.

[50] E.K. Yapp, R.I. Patterson, J. Akroyd, S. Mosbach, E.M. Adkins, J. Houston Miller, M. Kraft, Numerical simulation and parametric sensitivity study of optical band gap in a laminar co-flow ethylene diffusion flame, Combust. Flame 167 (2016) 320–334, doi:10.1016/j.combustflame.2016.01.033.

[51] V. Chernov, M.J. Thomson, S.B. Dworkin, N.A. Slavinskaya, U. Riedel, Soot formation with C1 and C2 fuels using an improved chemical mechanism for PAH growth, Combust. Flame 161 (2) (2014) 592–601, doi:10.1016/j.combustflame.2013.09.017.

[52] K. Nakaso, T. Fujimoto, T. Seto, M. Shimada, K. Okuyama, M.M. Lunden, Size distribution change of titania nano-particle agglomerates generated by gas phase reaction, agglomeration, and sintering, Aerosol Sci. Technol. 35 (2001) 929–947, doi:10.1080/02786820126857.

[53] P. Rodrigues, B. Franzelli, R. Vicquelin, O. Gicquel, N. Darabiha, Coupling an LES approach and a soot sectional model for the study of sooting turbulent non-premixed flames, Combust. Flame 190 (2018) 477–499, doi:10.1016/j.combustflame.2017.12.009.

[54] A. D'Anna, Detailed kinetic modeling of particulate formation in rich premixed flames of ethylene, Energy Fuels 22 (3) (2008) 1610–1619, doi:10.1021/ef700641u.

[55] A. D'Anna, J.H. Kent, R.J. Santoro, Investigation of species concentration and soot formation in a co-flowing diffusion flame of ethylene, Combust. Sci. Technol. 179 (1–2) (2007) 355–369, doi:10.1080/00102200600812419.

[56] C. Saggese, S. Ferrario, J. Camacho, A. Cuoci, A. Frassoldati, E. Ranzi, H. Wang, T. Faravelli, Kinetic modeling of particle size distribution of soot in a premixed burner-stabilized stagnation ethylene flame, Combust. Flame 162 (2015) 3356–3369, doi:10.1016/j.combustflame.2015.06.002.

[57] A. D'Anna, M. Sirignano, An advanced multi-sectional method for particulate matter modeling in flames, Green Energy and Technology, 2013, pp. 363–388.

[58] M. Sirignano, J. Kent, A. D'Anna, Further experimental and modelling evidences of soot fragmentation in flames, Proc. Combust. Inst. 35 (2) (2015) 1779–1786, doi:10.1016/j.proci.2014.05.010.

[59] S.H. Park, S.N. Rogak, W.K. Bushe, J.Z. Wen, M.J. Thomson, An aerosol model to predict size and structure of soot particles, Combust. Theory Model. 9 (2005) 499–513, doi:10.1080/13647830500195005.

[60] International Sooting Flame (ISF) Workshop (Accessed in 2016). URL http://www.adelaide.edu.au/cet/isfworkshop/.

[61] A. Cuoci, A. Frassoldati, T. Faravelli, E. Ranzi, Numerical modeling of laminar flames with detailed kinetics based on the operator-splitting method, Energy Fuels 27 (2013) 7730–7753, doi:10.1021/ef4016334.

[62] S.K. Friedlander, W.H. Marlow, Smoke, dust and haze: fundamentals of aerosol behavior, Phys. Today 30 (1977) 58–59, doi:10.1063/1.3037714.

[63] F. Bisetti, G. Blanquart, M.E. Mueller, H. Pitsch, On the formation and early evolution of soot in turbulent nonpremixed flames, Combust. Flame 159 (2012) 317–335, doi:10.1016/j.combustflame.2011.05.021.

[64] C. Schulz, B. Kock, M. Hofmann, H. Michelsen, S. Will, B. Bougie, R. Suntz, G. Smallwood, Laser-induced incandescence: recent trends and current questions, Appl. Phys. B 83 (3) (2006) 333–354, doi:10.1007/s00340-006-2260-8.

[65] H.A. Michelsen, Understanding and predicting the temporal response of laser-induced incandescence from carbonaceous particles, J. Chem. Phys. 118 (15) (2003) 7012–7045, doi:10.1063/1.1559483.

[66] H.A. Michelsen, F. Liu, B.F. Kock, H. Bladh, A. Boiarciuc, M. Charwath, T. Dreier, R. Hadef, M. Hofmann, J. Reimann, S. Will, P.E. Bengtsson, H. Bockhorn, F. Foucher, K.P. Geigle, C. Mounaïm-Rousselle, C. Schulz, R. Stirn, B. Tribalet, R. Suntz, Modeling laser-induced incandescence of soot: a summary and comparison of LII models, Appl. Phys. B: Lasers Opt. 87 (3) (2007) 503–521, doi:10.1007/s00340-007-2619-5.

[67] H. Bladh, J. Johnsson, P.E. Bengtsson, Influence of spatial laser energy distribution on evaluated soot particle sizes using two-colour laser-induced incandescence in a flat premixed ethylene/air flame, Appl. Phys. B: Lasers Opt. 96 (2009) 645–656, doi:10.1007/s00340-009-3523-y.

[68] H. Bladh, J. Johnsson, N.E. Olofsson, A. Bohlin, P.E. Bengtsson, Optical soot characterization using two-color laser-induced incandescence (2C-LII) in the soot growth region of a premixed flat flame, Proc. Combust. Inst, 33 (2011), pp. 641–648.

[69] B. Axelsson, R. Collin, P.-E. Bengtsson, Laser-induced incandescence for soot particle size measurements in premixed flat flames, Appl. Opt. 39 (2000) 3683, doi:10.1364/AO.39.003683.

[70] A. Cuoci, A. Frassoldati, T. Faravelli, E. Ranzi, OpenSMOKE++: an object-oriented framework for the numerical modeling of reactive systems with detailed kinetic mechanisms, Comput. Phys. Commun. 192 (2015) 237–264, doi:10.1016/J.CPC.2015.02.014.

[71] J. Zerbs, K.P. Geigle, O. Lammel, J. Hader, R. Stirn, R. Hadef, W. Meier, The influence of wavelength in extinction measurements and beam steering in laser-induced incandescence measurements in sooting flames, Appl. Phys. B: Lasers Opt. 96 (2009) 683–694, doi:10.1007/s00340-009-3550-8.

[72] R. Hadef, K.P. Geigle, W. Meier, M. Aigner, Soot characterization with laser-induced incandescence applied to a laminar premixed ethylene-air flame, Int. J. Thermal Sci. 49 (2010) 1457–1467.

[73] A.D. Abid, N. Heinz, E.D. Tolmachoff, D.J. Phares, C.S. Campbell, H. Wang, On evolution of particle size distribution functions of incipient soot in premixed ethylene-oxygen-argon flames, Combust. Flame 154 (2008) 775–788, doi:10.1016/j.combustflame.2008.06.009.

[74] A.D. Abid, E.D. Tolmachoff, D.J. Phares, H. Wang, Y. Liu, A. Laskin, Size distribution and morphology of nascent soot in premixed ethylene flames with and without benzene doping, Proc. Combust. Inst. 32 I (2009) 681–688, doi:10.1016/j.proci.2008.07.023.

[75] B. Zhao, Z. Yang, Z. Li, M.V. Johnston, H. Wang, Particle size distribution function of incipient soot in laminar premixed ethylene flames: effect of flame temperature, Proc. Combust. Inst. 30 (2005) 1441–1448, doi:10.1016/j.proci.2004.08.104.

[76] C. Betrancourt, F. Liu, P. Desgroux, X. Mercier, A. Faccinetto, M. Salamanca, L. Ruwe, K. Kohse-Höinghaus, D. Emmrich, A. Beyer, A. Gölzhäuser, T. Tritscher, Investigation of the size of the incandescent incipient soot particles in premixed sooting and nucleation flames of n-butane using LII, HIM, and 1 nm-SMPS, Aerosol Sci. Technol. 51 (2017) 916–935, doi:10.1080/02786826.2017.1325440.

[77] S. De Iuliis, S. Maffi, F. Cignoli, G. Zizak, Three-angle scattering/extinction versus TEM measurements on soot in premixed ethylene/air flame, Appl. Phys. B: Lasers Opt. 102 (2011) 891–903, doi:10.1007/s00340-010-4344-8.

[78] N.J. Kempema, M.B. Long, Combined optical and TEM investigations for a detailed characterization of soot aggregate properties in a laminar coflow diffusion flame, Combust. Flame 164 (2016) 373–385, doi:10.1016/j.combustflame.2015.12.001.
[79] Sooting Yale coflow diffusion flames database (Accessed in 2016). http://guilford.eng.yale.edu/yalecoflowflam.
[80] M.D. Smooke, R.J. Hall, M.B. Colket, J. Fielding, M.B. Long, C.S. McEnally, L.D. Pfefferle, Investigation of the transition from lightly sooting towards heavily sooting co-flow ethylene diffusion flames, Combust. Theory Model. 8 (3) (2004) 593–606, doi:10.1088/1364-7830/8/3/009.
[81] B. Franzelli, M. Roussillo, P. Scouflaire, J. Bonnety, R. Jalain, T. Dormieux, S. Candel, G. Legros, Multi-diagnostic soot measurements in a laminar diffusion flame to assess the ISF database consistency, Proc. Combust. Inst. (2018), doi:10.1016/j.proci.2018.05.062.
[82] C.S. Wen, The fundamentals of aerosol dynamics, World Scientific, 1996, doi:10.1142/3101.
[83] F. Liu, H. Guo, G.J. Smallwood, Ö.L. Gülder, Effects of gas and soot radiation on soot formation in a coflow laminar ethylene diffusion flame, J. Quant. Spectrosc. Radiat. Transf. 73 (2002) 409–421, doi:10.1016/S0022-4073(01)00205-9.
[84] H. Guo, F. Liu, G.J. Smallwood, Ö.L. Gülder, The flame preheating effect on numerical modelling of soot formation in a two-dimensional laminar ethylene-air diffusion flame, Combust. Theory Model. 6 (2002) 173–187, doi:10.1088/1364-7830/6/2/301.
[85] P.B. Kuhn, B. Ma, B.C. Connelly, M.D. Smooke, M.B. Long, Soot and thin-filament pyrometry using a color digital camera, Proc. Combust. Inst. 33 (2011) 743–750, doi:10.1016/j.proci.2010.05.006.
[86] M.D. Smooke, M.B. Long, B.C. Connelly, M.B. Colket, R.J. Hall, Soot formation in laminar diffusion flames, Combust. Flame 143 (2005) 613–628, doi:10.1016/j.combustflame.2005.08.028.
[87] B.C. Connelly, M.B. Long, M.D. Smooke, R.J. Hall, M.B. Colket, Computational and experimental investigation of the interaction of soot and NO in coflow diffusion flames, Proc. Combust. Inst. 32 I (1) (2009) 777–784, doi:10.1016/j.proci.2008.06.182.
[88] J.D. Herdman, B.C. Connelly, M.D. Smooke, M.B. Long, J.H. Miller, A comparison of Raman signatures and laser-induced incandescence with direct numerical simulation of soot growth in non-premixed ethylene/air flames, Carbon 49 (15) (2011) 5298–5311, doi:10.1016/j.carbon.2011.07.050.
[89] A. Khosousi, S.B. Dworkin, Detailed modelling of soot oxidation by O_2 and OH in laminar diffusion flames, Proc. Combust. Inst. 35 (2) (2015) 1903–1910, doi:10.1016/j.proci.2014.05.152.
[90] C. Saggese, N.E. Sánchez, A. Frassoldati, A. Cuoci, T. Faravelli, M.U. Alzueta, E. Ranzi, Kinetic modeling study of polycyclic aromatic hydrocarbons and soot formation in acetylene pyrolysis, Energy Fuels 28 (2) (2014) 1489–1501, doi:10.1021/ef402048q.
[91] C. Saggese, A. Cuoci, A. Frassoldati, S. Ferrario, J. Camacho, H. Wang, T. Faravelli, Probe effects in soot sampling from a burner-stabilized stagnation flame, Combust. Flame 167 (2016) 184–197, doi:10.1016/j.combustflame.2016.02.013.
[92] C. Saggese, A. Frassoldati, A. Cuoci, T. Faravelli, E. Ranzi, A wide range kinetic modeling study of pyrolysis and oxidation of benzene, Combust. Flame 160 (7) (2013) 1168–1190, doi:10.1016/j.combustflame.2013.02.013.
[93] E. Ranzi, A. Frassoldati, R. Grana, A. Cuoci, T. Faravelli, A. Kelley, C. Law, Hierarchical and comparative kinetic modeling of laminar flame speeds of hydrocarbon and oxygenated fuels, Prog. Energy Combust. Sci. 38 (4) (2012) 468–501, doi:10.1016/j.pecs.2012.03.004.
[94] E. Cenker, K. Kondo, G. Bruneaux, T. Dreier, T. Aizawa, C. Schulz, Assessment of soot particle-size imaging with LII at diesel engine conditions, Appl. Phys. B: Lasers Opt. 119 (4) (2015) 765–776, doi:10.1007/s00340-015-6106-0.
[95] K.K. Foo, Z. Sun, P.R. Medwell, Z.T. Alwahabi, B.B. Dally, G.J. Nathan, Experimental investigation of acoustic forcing on temperature, soot volume fraction and primary particle diameter in non-premixed laminar flames, Combust. Flame 181 (2017) 270–282, doi:10.1016/j.combustflame.2017.04.002.